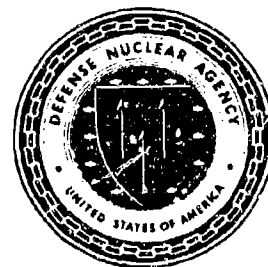Defense Nuclear Agency
Alexandria, VA 22310-3398

AD-A286 380
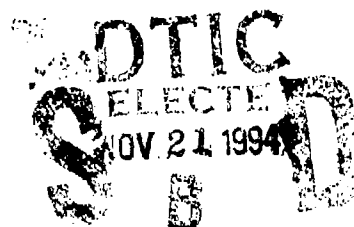
Soft X-Ray Innovative Source Development Program

Edward J. Yadlowsky, et al.
HY-Tech Research Corp.
104 Centre Court
Radford, VA 24141

DTIC
ELECTE
NOV 21 1994
B

November 1994

Technical Report

94-35602

6

Destroy this report when it is no longer needed Do not return to sender

DISTRIBUTION LIST UPDATE

This mailer is provided to enable DNA to maintain current distribution lists for reports (We would appreciate your providing the requested information.)

☐ Add the individual listed to your distribution list

☐ Delete the cited organization/individual

☐ Change of address

NAME _____

ORGANIZATION _____

OLD ADDRESS	CURRENT ADDRESS
_____	_____
_____	_____
_____	_____

TELEPHONE NUMBER ( ) _____

DNA PUBLICATION NUMBER/TITLE	CHANGES/DELETIONS/ADDITIONS, etc.) (Attach Sheet if more Space is Required)
_____	_____
_____	_____
_____	_____

DNA OR OTHER GOVERNMENT CONTRACT NUMBER: _____

CERTIFICATION OF NEED-TO-KNOW BY GOVERNMENT SPONSOR (if other than DNA):

SPONSORING ORGANIZATION: _____

CONTRACTING OFFICER OR REPRESENTATIVE: _____

SIGNATURE _____

CUT HERE AND RETURN

REPORT DOCUMENTATION PAGE

Public reporting burden for this collection of information is estimated to average 1 hour per response including the time for reviewing instructions, searching existing data sources, gathering and maintaining the data needed, and completing and reviewing the collection of information. Send comments regarding this burden estimate or any other aspect of this collection of information including suggestions for reducing this burden , to Washington Headquarters Services Directorate for Information Operations and Reports, 1215 Jefferson Davis Highway, Suite 1204, Arlington, VA 22202-4302, and to the Office of Management and Budget, Paperwork Reduction Project (0704-0188), Washington, DC 20503

1. AGENCY USE ONLY (Leave blank)	2. REPORT DATE	3. REPORT TYPE AND DATES COVERED
	941101	Technical 890324 – 930712

4. TITLE AND SUBTITLE	5. FUNDING NUMBERS
Soft X-Ray Innovative Source Development Program	C -DNA 001-89-C-0029 PE -62715H PR -RL TA -RB WU-DH053570
6. AUTHOR(S) Edward J. Yadlowsky, John J. Moschella, Robert C. Hazelton and Thomas B. Settersten	

7 PERFORMING ORGANIZATION NAME(S) AND ADDRESS(ES)	8. PERFORMING ORGANIZATION REPORT NUMBER
HY-Tech Research Corp. 104 Centre Court Radford, VA 24141	015FR

9 SPONSORING/MONITORING AGENCY NAME(S) AND ADDRESS(ES)	10. SPONSORING/MONITORING AGENCY REPORT NUMBER
Defense Nuclear Agency 6801 Telegraph Road Alexandria, VA 22310-3398 RAST/Hebert	DNA-TR-93-190

11. SUPPLEMENTARY NOTES

This work was sponsored by the Defense Nuclear Agency under RDT&E RMC Code B4662D RL RB 00078 RAEV 3300A AF 25904D.

12a. DISTRIBUTION/AVAILABILITY STATEMENT	12b. DISTRIBUTION CODE
Approved for public release; distribution is unlimited.	

13. ABSTRACT (Maximum 200 words)

Recent models predict that individual wires in an array will form heterogeneous current channels when exploded by a current pulse. The resulting non uniform magnetic forces will cause the outer current carrying corona to implode ahead of the core, in contrast to earlier models where the uniform current channel implodes as a unit. Laser based absorption and holographic techniques have been used to study the explosion characteristics of 33 μm C and 25 μm Al wire loads and the implosion dynamics of two wire Al loads on a 300 kA generator. X-ray techniques have been used to study the implosion and radiation characteristics of Mg coated Al wire arrays on the 4 MA Double Eagle generator. The high resolution laser diagnostics reveal a coronal plasma that implodes far in advance of the core in the two wire experiments. This preemptive implosion of the corona is exacerbated when a POS shortens the current pulse. The Mg coated Al wire load experiments indicate that only the outer 30-50% of the load mass implodes to radiate in the K-shell. The load straggling implies a softened implosion and reduced radiation efficiency. The results demonstrate the importance of the early time current distribution on the implosion and radiation characteristics of the load and underscore the need for adequate modeling to scale present results up to larger machines.

14. SUBJECT TERMS		15. NUMBER OF PAGES
Implosion Wire Array POS Coronal Plasma K-Shell		92
		16. PRICE CODE

17. SECURITY CLASSIFICATION OF REPORT	18. SECURITY CLASSIFICATION OF THIS PAGE	19. SECURITY CLASSIFICATION OF ABSTRACT	20 LIMITATION OF ABSTRACT
UNCLASSIFIED	UNCLASSIFIED	UNCLASSIFIED	SAR

CLASSIFIED BY:

N/A since Unclassified.

DECLASSIFY ON:

N/A since Unclassified.

CONVERSION TABLE

Conversion factors for U. S. Customary to metric (SI) units of measurement

MULTIPLY ────────────→ BY ────────────→ TO GET

TO GET ←──────────── BY ←──────────── DIVIDE

angstrom	1.000 000 X E -10	meters (m)
atmosphere (normal)	1.013 25 X E +2	kilo pascal (kPa)
bar	1.000 000 X E +2	kilo pascal (kPa)
barn	1 000 000 X E -28	meter^2 (m^2)
British thermal unit (thermochemical)	1.054 350 X E +3	joule (J)
calorie (thermochemical)	4.184 000	joule (J)
cal (thermochemical)/cm^2	4.184 000 X E -2	mega joule/m^2 (MJ/m^2)
curie	3.700 000 X E +1	*giga becquerel (GBq)
degree (angle)	1.745 329 X E -2	radian (rad)
degree Fahrenheit	$T_K = (T\,^\circ F + 459.67)/1.8$	degree kelvin (K)
electron volt	1.602 19 X E -19	joule (J)
erg	1.000 000 X E -7	joule (J)
erg/second	1.000 000 X E -7	watt (W)
foot	3.048 000 X E -1	meter (m)
foot-pound-force	1.355 818	joule (J)
gallon (U.S. liquid)	3.785 412 X E -3	meter^3 (m^3)
inch	2.540 000 X E -2	meter (m)
jerk	1.000 000 X E +9	joule (J)
joule/kilogram (J/kg) (radiation dose absorbed)	1.000 000	Gray (Gy)
kilotons	4.183	terajoules
kip (1000 lbf)	4.448 222 X E +3	newton (N)
kip/inch^2 (ksi)	6.894 757 X E +3	kilo pascal (kPa)
ktap	1.000 000 X E +2	newton-second/m^2 (N-s/m^2)
micron	1.000 000 X E -6	meter (m)
mil	2.540 000 X E -5	meter (m)
mile (international)	1.609 344 X E +3	meter (m)
ounce	2.834 952 X E -2	kilogram (kg)
pound-force (lbs avoirdupois)	4.448 222	newton (N)
pound-force inch	1.129 848 X E -1	newton/meter (N m)
pound-force/inch	1.751 268 X E +2	newton-meter (N/m)
pound-force/foot^2	4.788 026 X E -2	kilo pascal (kPa)
pound-force/inch^2 (psi)	6.894 757	kilo pascal (kPa)
pound-mass (lbm avoirdupois)	4.535 924 X E -1	kilogram (kg)
pound-mass-foot^2 (moment of inertia)	4.214 011 X E -2	kilogram-meter^2 (kg-m^2)
pound-mass-foot^3	1 601 846 X E +1	kilogram/meter^3 (kg/m^3)
rad (radiation dose absorbed)	1.000 000 X E -2	**Gray (Gy)
roentgen	2.579 760 X E -4	coulomb/kilogram (C/kg)
shake	1.000 000 X E -8	second (s)
slug	1.459 390 X E +1	kilogram (kg)
torr (mm Hg, 0° C)	1.333 22 X E -1	kilo pascal (kPa)

*The becquerel (Bq) is the SI unit of radioactivity; 1 Bq = 1 event/s
**The Gray (Gy) is the SI unit of absorbed radiation

TABLE OF CONTENTS

TABLE OF CONTENTS (Continued)

FIGURES

FIGURES (Continued)

SECTION 1

INTRODUCTION

Extensive studies have been carried out in an attempt to achieve very high density and high temperature plasma conditions by passing large currents through a wide variety of loads.[1] These Z-pinch plasmas are of interest as sources of x-rays, potential thermonuclear reactors, and an optical pump for x-ray laser application, to mention a few. Very important issues confronting the researchers trying to achieve these energetic plasma conditions is the efficiency of coupling the generator to the load, the stability of the load, the dynamics of the load during the implosion phase and the heating and radiating processes occurring after the load stagnates on axis.

Various load configurations have been attempted to address one or more of these issues. Annular wire arrays and gas puffs have attempted to improve the coupling efficiency by reducing load impedance relative to a single wire load.[2] Load stability has been sought by employing a series of nested gas puffs to reduce the disruptive effect of Rayleigh-Taylor instabilities,[3] and using an axial magnetic field on axis to suppress MHD sausage instabilities.[4] Improved stability and coupling efficiency were also reported recently when a gas puff source was imploded onto a wire load.[5]

Improved load performance has also been sought using pulse forming lines and plasma opening switches (POS) to shorten the current pulse rise time.[6] The large $\dot{I} = dI/dt$ of these devices is expected to increase the kinetic energy of the imploding load and achieve implosion before disruptive plasma instabilities occur. The rapid $\dot{I}$ has been predicted to quickly form a conducting sheath around each vaporized and ionized wire element in the array.[7] The magnetic force then prevents the wire from expanding, allowing each element to implode as a unit onto the axis without shorting to the return current posts.

Although great progress has been made in understanding the physical processes occurring in these dense Z-pinch devices many important questions still remain. Optimum yield is predicted to occur if the load implodes on axis when the current reaches its peak value and the kinetic energy per ion is sufficient to reach the K-shell ionization level.[8] The conditions for optimum x-ray yield are in reasonable agreement with the prediction. However, the observed x-ray pulse duration is an order of magnitude larger than predicted and the observed yield

1

is correctly predicted only if the radiating mass is, in general, assumed to be only a small fraction of the initial wire mass.[8] The results from experiments on numerous machines indicates that the optimum yield is observed when the initial wire diameter is 0.025 μm, a result that is not understood.[9] The enhanced pulse length and smaller than expected assembled mass both suggest straggling in the load assembly on axis with some fraction of the mass arriving after the main emission event. In addition, the kinetic energy of implosion only accounts for $\frac{1}{3}$ of the radiated energy, indicating a nonOhmic heating occurs after the load assembles on axis. The origin of this heating has not been determined.[10]

The assumption that the wire loads quickly vaporize and ionize into a highly conducting plasma may not be valid even for very rapid current rise times. Lindenmuth et al. [11] and Bobrova et al.[12] have attributed the stability of frozen D_2 fiber load experiments to a persistent solid core and Aranchuck et al.[13] have attributed the CuK$_\alpha$ emission that they observe to electrons hitting a residual solid Cu core. The observation, by Aivosov et al.,[14] of a precursor plasma assembling on axis before the main array arrives further supports the concept of a multi-phase current channel which allows a low mass coronal plasma to separate from the main channel and implode prematurely. The importance of the initial conditions occurring on each wire is further underscored by the observations of R. Spielman that superior plasma radiation source (PRS) performance is achieved if a 300 ns prepulse is added to the very short rise time pulse (60 ns) of the Saturn generator.[10]

The study described herein addresses these issues of initial plasma condition, precursor plasma formation, plasma load preconditioning, and the effect of $\dot{I}$ on the coupling of the generator to the load and on plasma stability.

The studies were carried out on a number of generator configurations. A 7.8 μF capacitor bank was used to deliver a sinusoidal current to the load with peak amplitudes in the range of 300-375 kA with a quarter period of 1.2-1.4 μs. In some studies a 2.5 nF capacitor delivering a 0.5 J pulse was fired 0.3-1 μs before the main bank to vaporize and preionize the load prior to application of the main current pulse. A plasma opening switch (POS) was used to shorten the current rise time to about 100 ns and increase $\dot{I}$ from 0.2 x 10^{12} A/s observed with the main bank only to 1 x 10^{12} A/s with the POS. This later value is comparable to the $\dot{I}$ per wire obtained on the Double Eagle generator driving a 20 wire load. Studies were also carried out on the Double Eagle generator delivering 4 MA to a 12 wire load in 100 ns.

These studies were extensively diagnosed using streaked emission and absorption photography to study load dynamics, holographic interferometry to study plasma channel formation, and x-ray pinhole photography to identify the radiating regions in the plasma. Multiple pinhole cameras employing gated microchannel plates were used to study the temporal evolution of the radiating volume where as the open shutter variety were used to monitor the

2

average emission characteristics. Filtered gallium arsenide photoconducting diodes (GAD) were used to record the x-ray intensity and magnetic pickup-loops were used to monitor the feedline and load currents.

The debris emitted by the discharge was collected on quartz slides and analyzed with a scanning electron microscope. The studies carried out on Double Eagle also had a crystal spectrometer, and a gated grazing incidence spectrometers (McPigs) to determine the spectrum of emitted x-rays.

A variety of loads were studied from single fiber/wire carbon or aluminum loads to wire arrays consisting of multiple coated loads. Carbon fibers were considered for this study because this low Z element should be readily stripped to the K-shell even with the modest currents in HY-Tech's White lit'nin facility. The difference in the vaporization properties and conductivities of Al and C provided an avenue for studying the effect of initial conditions on current channel formation. Two wires oriented perpendicular to the probing laser provided a clear view of the interwire region for studying implosion dynamics and precursor plasma formation.

Composite loads consisting of layers of different elements were studied to evaluate the stability and coupling efficiency that could be achieved by mixing high and low Z elements. Studies have shown that better compression ratio and enhanced pinch stability could be achieved by adding 5% Xe to a H_2 gas puff plasma.[15] The radiative properties of high Z elements are expected to promote the compression of individual wires in the array by reducing the temperature and hence pressure causing them to expand. The tightly pinched elements could then implode without producing a significant precursor plasma. By avoiding a precursor plasma that can implode ahead of the array and soften the implosion, more efficient coupling of the generator to the load can be achieved. The spectral content of the emitted radiation can also be tailored by a judicious combination of elements. Finally, the layered loads provide an opportunity to obtain radially resolved information about the current channel. By measuring when and where the L or K-shell spectra of the various elements light-up, the time of arrival and temperature of the stagnating load can be probed.

The highly magnified spatially and temporally resolved diagnostics used in this study reveal many new and significant features not seen before.

1. A multiphase plasma/current channel is formed with a low density coronal plasma surrounding a dense core which is only partially ionized well into the current pulse. The coronal plasma is a highly conducting shell that responds to the magnetic field and may be the main current conducting channel. This coronal plasma appears to be due to out gassed or vaporized material blown off the wire or fiber surface.

2. The soft x-ray portion ($E \leq 0.3$ keV) of the spectrum appears to come from hollow

3

shells outside the interior core. These shells appear to be associated with the coronal plasma. The hard x-rays ($E \geq 1$ keV) radiate from small "hot spots" which appear to be located near the original wire position.

3. The generator appears to couple to the load more efficiently when no POS is used to shorten the pulse.

4. The coronal plasma is observed to separate from the central core and implode in the two wire experiments. This separation and ensuing straggling appears to be more severe when a POS shortens the current rise time.

5. The total K-shell yield of Mg coated Al loads is observed to peak for a 20%, by mass, Mg coating.

6. The fraction of Al that is on-axis during the K-shell radiation pulse goes to zero when the mass of the Mg coating approaches 50%.

7. Theoretical calculations show a low density coronal plasma having 9% of the load mass surrounding a cold core. This corona conducts 70% of the load current even though its density may be only 10^{-4} of the core density.

The results obtained in this study are consistent with the observations of others and may explain other phenomena that are presently considered anomalous. They agree with the predictions of multiphase plasma channels by Lindenmuth *et al.* and others,[11, 12, 16] and the observations of Aranchuk *et al.* and Figura *et al.*.[13, 17] The separation of the coronal plasma from the neutral core and its subsequent implosion observed in two wire experiments confirms the measurements made by Aivozov *et al.* concerning precursor plasma formation.[14] This phenomena may account for lower than anticipated yields due to a softened load implosion, which compresses a small fraction of the mass radiating on axis in the K-shell,[8] and the longer than anticipated radiation pulse length.[8] The more efficient coupling of the generator to the load observed without the POS (lower $\dot{I}$) may explain why a current prepulse on the Saturn generator produces superior yields with PRS loads.

These results have significant consequences for the chances of achieving desired radiation yields on the Jupiter and next generation of simulators. First and foremost, the initial conditions in the load are very important to the subsequent implosion of the load. Multiphase discharge channel formation will result in very nonuniform plasmas distribution on foil loads. These nonuniformities are the seeds for Raleigh-Taylor instabilities, and have been identified as the most serious obstacles to good foil implosion on Pegasus and Shiva Star.[18, 19] It clearly suggests that good uniform vaporization and ionization of the load should be accomplished before the main current pulse is applied. It further suggests that the initial plasma formation must be adequately modelled before realistic theoretical predictions can be made. The scaling laws derived from predictions that have been bench marked by experiment, are

4

necessary for the design of future machines.

The next chapter presents the calculated evaluation of an aluminum coated carbon fiber load using a 1-D hydrodynamic model. The experimental system is described in Section 3 and the results are presented in Section 4. A discussion of these results then follows and a conclusion chapter completes the report.

SECTION 2
THEORY

2.1 INTRODUCTION.

Numerical simulations of pulsed power driven Z-pinch plasmas almost universally start with the load in a preheated plasma state. The rationale for introducing this initial plasma state is to avoid addressing the complex physics issues associated with the early time plasma formation due to primary induced current breakdown. To describe primary induced current breakdown would require addressing, at a minimum, such questions as: where is the current flowing and what is its distribution, how does the cold matter resistivity vary with temperature and density, and how does one describe and characterize the equations of state and transport properties through phase changes as the wire heats up. Without this information it is unclear how the early time plasma formation influences the wire dynamics and ultimately the radiative yield. Some of the issues surrounding the cold start problem were previously investigated. [7] One of the conclusions reached in that investigation was that the later time behavior of the plasma is relatively insensitive to the details of the initial conditions. The analysis was based on a similarity solution of the hydrodynamic expansion and consisted of a single zone with an average temperature as a function of time. 0-D single zone simulations are often used to provide guidance and indicate trends, but because of the use of a single temperature, 0-D models are, at best, crude estimates. Although the early time phenomenology predicted by this model is in qualitative agreement with some gross experimental features for a single wire it does not provide satisfactory quantitative agreement nor does it provide any detailed spectral information. In the absence of any real hard data for comparison, it is difficult to generalize that the early time behavior is uncoupled from the later time radiative efficiency and performance. Also, for wire arrays and puff gas plasmas there is evidence to support the notion that there is coupling between early and late-time phenomenology. The first example comes from an investigation comparing the radiative yields from a wire array as a function of initial wire diameter.[20] In this paper it was found that there was an optimum wire radius corresponding to the highest radiative yield. Another well known theoretical example arises simply because variations in the pressures opposing the driving magnetic pis-

6

ton that, in the course of events, affects the dynamics and ultimately the radiative yield. In addition there is the question concerning all the issues regarding the transport of energy and momentum in the plasma for a given current distribution. In the past, most, if not all, of the investigations assumed the plasma could be represented a a laminar MHD plasma flow with classical transport coefficients. However, it has long been known that the plasma exhibits turbulent behavior during its evolution which has usually been accounted for by introducing arbitrary anomalous transport coefficients into the model. In addition, it must be remembered that since the early time behavior is critically dependent on the equation of state as the wire material undergoes phase changes, which subsequently affects the resistivity, the heating and dynamics will also be affected. These issues must be addressed in the future if we are to understand all aspects of load dynamics in order to improve load performance and enhance yields. For the present, these issues are beyond the scope and intention of this investigation and will not be addressed here. We will adopt a much simpler approach and focus only in the differences in the early time plasma behavior due to the introduction of a non-classical resistivity and investigate how it influences observed phenomenon such as the early time dynamics and emission spectra. In the past, anomalous resistivity was accounted for by multiplying Spitzer resistivity by a variety of multiplicative factors in order to obtain agreement with the radiative yields. The approach adopted here is to employ a theoretically derived non-classical resistivity rather than search for some multiplication factor. A comparison will then be made between numerically simulated emission spectra and profiles of the plasma during the first 100 ns of the current pulse for Spitzer and non-Spitzer resistivity.

2.1.1 Model.

The numerical simulations are carried out with a 1-D non-LTE radiation hydrodynamics model self-consistently coupled to the external circuit equation a Pithon-class generator. For a given voltage profile the model self-consistently generates a current profile shown in Figure 2-1. The load is modeled as a single wire composed of an inner carbon fiber (14 μ radius) concentrically surrounded by an outer coating of aluminum (1 μ thick). The wire length is taken as 3 cm long but all results are given per cm. The atomic model contains all the ground states of carbon and aluminum and an excited state manifold for both materials in order to account adequately for the spectral diagnostics and, for the later times, the radiative energetics. The radiation transport model uses a probability of escape method with a multi-zone capability. In the benchmark simulation the electrical resistivity is represented by a Spitzer formula since it is the expression most commonly employed in the majority of calculations. The second simulation employs an expression for the resistivity that is valid

7

over a wider range of parameter space including the dense cold plasma. It is well known that this form of the resistivity does not transition into Spitzer at higher temperatures and lower densities as shown in Figure 2-2. This difference is well known in the literature. (see, for example, [21])

2.1.2   Results.

For the voltage profile shown in Figure 2-1 a self-consistent current was calculated using the circuit model. Since this report is concerned only with the first 100 ns or so, the current rises to a value of about 0.6 MA. However, this is more than sufficient to characterize the initial start-up plasma. The early time evolution of a single wire driven by a rapidly rising current exhibits three stages: heating, expansion, and contraction. The wire is first ohmically heated; is then followed by an expansion phase and subsequently enters a contraction phase. Initially, when the resistivity is high the wire is heated. This is followed by an expansion phase so long as the fluid pressure exceeds the magnetic pressure. When the magnetic pressure becomes greater than the fluid pressure the plasma enters its contraction phase and implodes onto its axis For the classical case (Spitzer) the resistivity increases with decreasing temperature (i.e. in the absence of a component due to the electron-neutral collision frequency). For the nonclassical expression used here the resistivity will first increase at low temperatures and then decrease as the temperature increases. This difference will manifest itself in the early time phenomenology. There is also an unresolved problem plaguing the early time cold start problem that involves the determination of the effective charge at low temperature. Since there is an uncertainty in our knowledge of the effective charge there also exists an uncertainty in the resistivity and that can lead to significant errors in characterizing the cold start problem. Just how large an effect this will have on the current distribution during the heating phase will have to await a sensitivity analysis involving the effects of ionization lowering and equation of state calculation.

The simulations presented here are identical in every respect except for the treatment of the electrical resistivity. In the first set of simulations, referred to as the Benchmark calculation, classical Spitzer resistivity (the "B" curve) was used. The load consists of an inner carbon fiber with a radius of 14 μm while the thickness of the concentric aluminum overcoat is 1 μm. The electrical conductivity used in these computations is shown in Figure 2-2 as a function of temperature and for one density. There are two curves with the Spitzer label: the "A" curve represents the conventional Spitzer conductivity with a $\log\lambda=5$ cutoff. The "B" curve represents the Spitzer-Harm-like conductivity with a $\log\lambda=5$ cutoff. The "B" form of the classical conductivity was used. The curve labeled "Cauble" represents a non

8
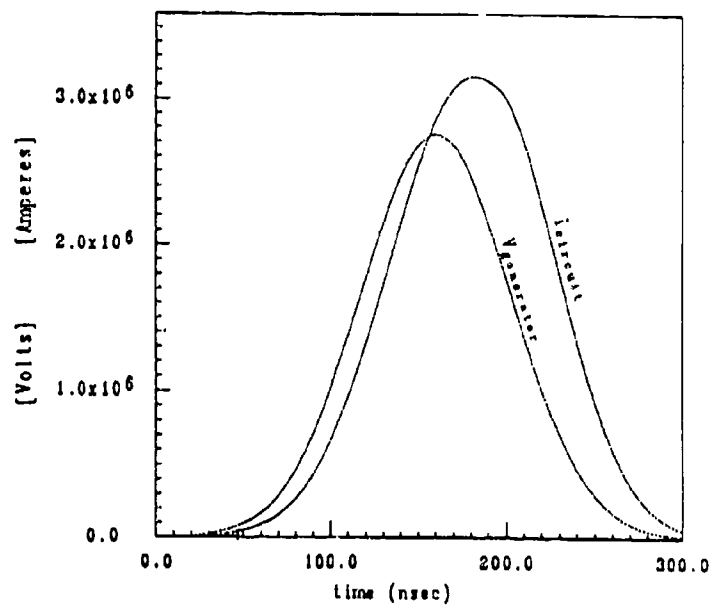
Figure 2-1. Voltage and current waveforms.
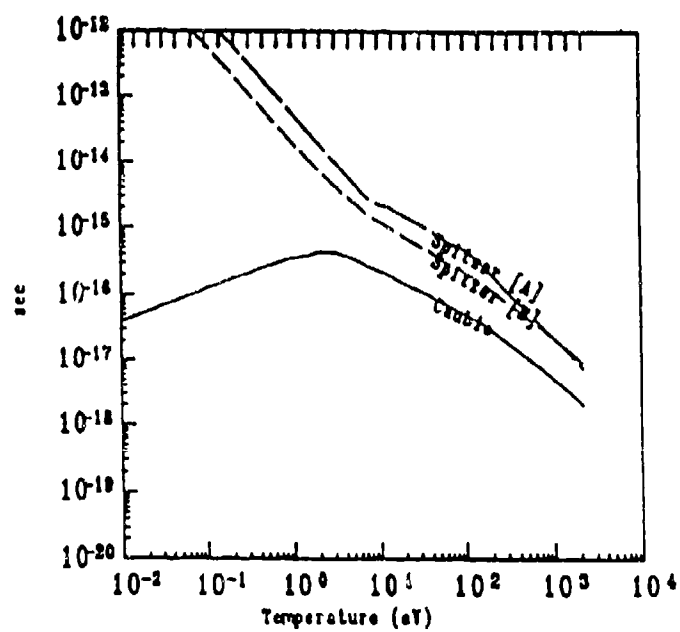
Figure 2-2. Temperature dependence of the three models for the resistivity of the plasma at one value of the mass density.

9

classical conductivity.[22]

2.2 BENCHMARK SIMULATION.

The evolution of the wire plasma using Spitzer conductivity has been calculated for the first 100 ns of the plasmas' evolution. A summary of these results are shown on Figure 2-3 and 2-4. Figure 2-3 represents a history of the energy and its components as a function of time. The "Total" energy represents the sum total of all the components. The "Plasma" energy represents the sum of the kinetic, ionization, and thermal energy. During the early time heating phase the thermal energy and energy stored in ionization account for most of the energy. At about 90 ns the radiative energy exceeds the thermal energy and begins to dominate the energetics of the single wire. The kinetic energy component plays a minor role in the overall energetics of a single wire. However, as shown in Figure 2-3 the kinetic energy exhibits an oscillatory behavior representative of expansions and contractions reminiscent of a Bennett-like equilibrium pinch. Representative profiles of the plasma temperature, density, current density, pressure, and emission spectrum are presented in Figure 2-4 at $t \simeq 40$ ns when the load current is 25-35 kA. A warm corona surrounding a cold core is observed throughout the entire wire/plasma evolution. Even though this corona contains only $\sim 9\%$ of the load mass, it conducts 70% or more of the load current.

2.3 NONCLASSICAL RESISTIVITY.

The corresponding energy history and hydrodynamic profile obtained with the Cauble resistivity are presented in Figures 2-5 and 2-6. Qualitatively there does not appear to be large energetic differences in comparison with the benchmark simulation. However, a closer scrutiny of Figure 2-5 shows some interesting phenomenological differences. First, the kinetic energy undergoes more oscillations during the first 60 ns of the run. This is a reflection of the variation of dL/dt due to the variation of the radius and the increasing magnetic field during the current rise. Also, the appearance of the "peak" or slight enhancement in the thermal energy, which coincides with the increased heating due to compression, followed by the contraction occurs earlier in time than for the benchmark calculation.
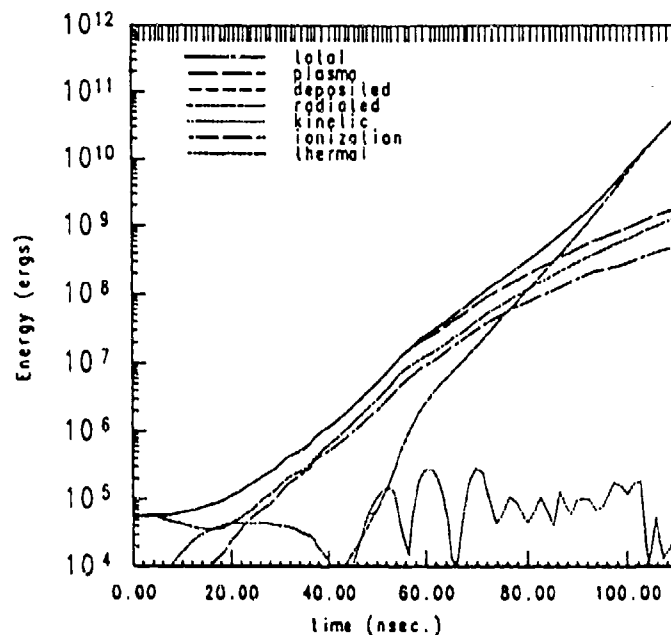
Figure 2-3. Energy history as a function of time using classical Spitzer-Harm plasma resistivity model.
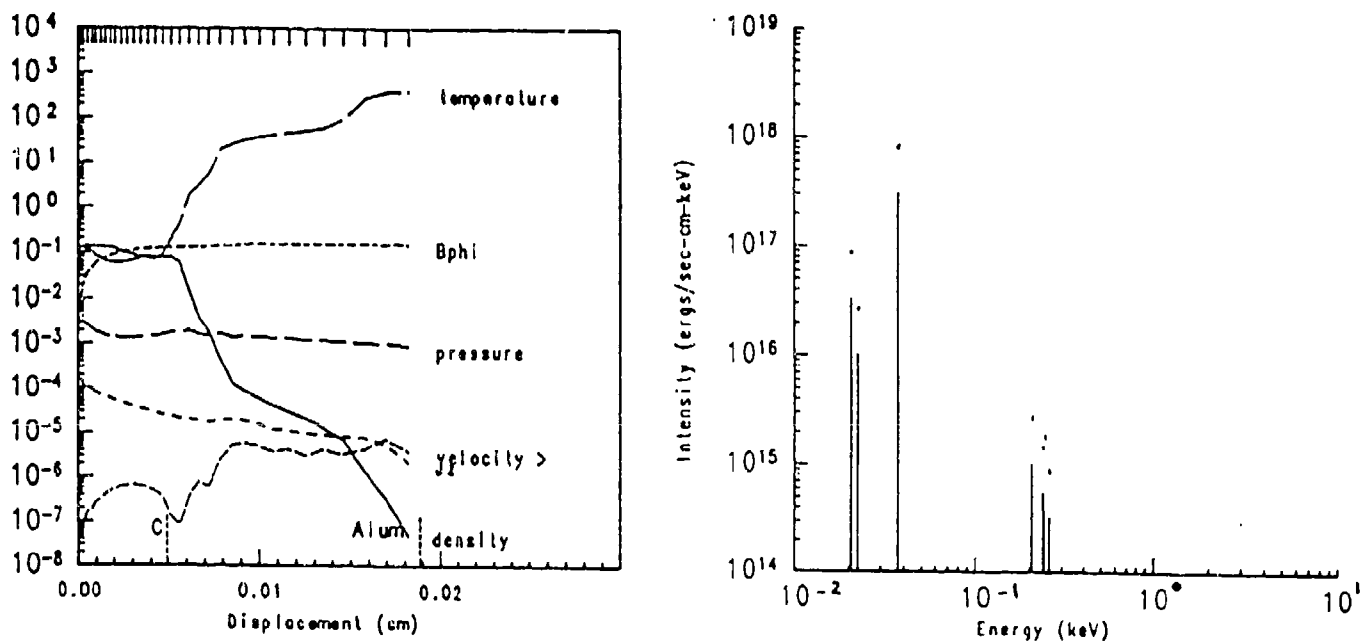
Figure 2-4. Radial profiles of plasma quantities and emission spectrum calculated with classical Spitzer-Harm resistivity model.

11
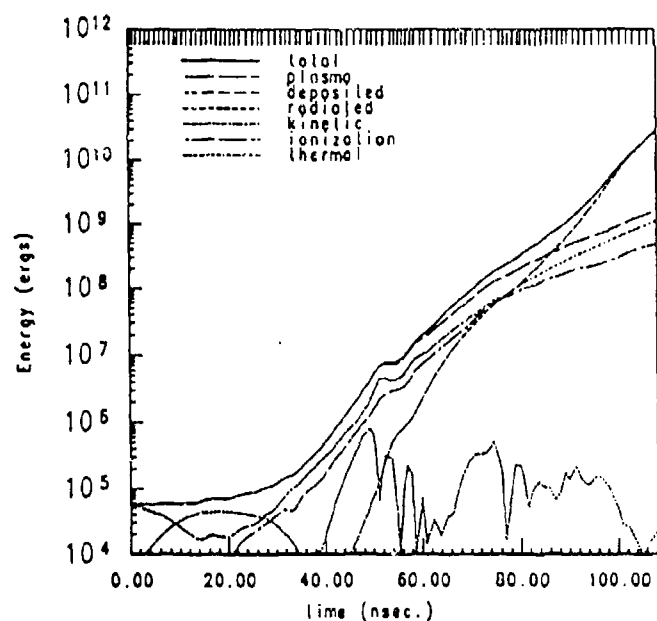
Figure 2-5. Energy history as a function of time using Cauble resistivity model.
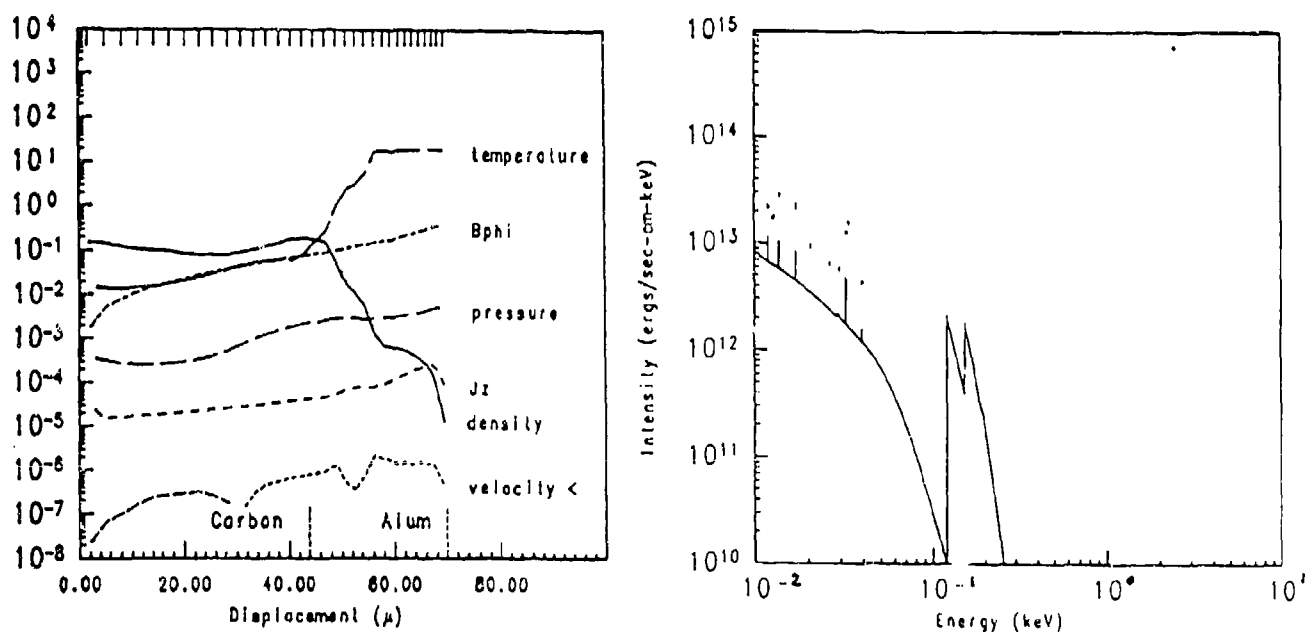
Figure 2-6. Radial profiles of plasma quantities and emission spectrum calculated with the Cauble resistivity model.

2.4 SUMMARY.

During the first 100 ns there are observable differences in the energetics and radius as a function of time between the two cases investigated. There are significant and observable differences in the emitted spectra both in magnitude and in the appearance of the specific spectral lines as a function of time. The magnitude of the continuum radiation is also observably different, particularly at very early times. With state-of-the-art spectroscopy and interferometry it should be possible to differentiate between the two cases when unfolding experimental data by observing the time delay in the emission of selected fiducial carbon lines as a function of the overcoat thickness. However, it should be pointed out that the experimental results contain the combined integrated action of a variety of phenomena occurring simultaneously. This makes it essential to theoretically investigate the consequences of each phenomena separately as well as collectively in order to determine how each affects the final result.

The numerical simulations presented here have focused on a single issue for an idealized situation in the sense that a particular form of the conductivity was adopted. It is obviously a first attempt to self-consistently calculate the dynamics based on an expression for the conductivity that extends over a broad temperature range, particularly for low temperatures. Clearly, there is a need to develop an improved theory to deal with the issue of conductivity and, for that matter, all the transport issues mentioned in the Introduction. Incorporating these effects into the model will permit a systematic study of the wire phenomenology and better correlate the relationship between the early and late time behavior as well as the experimental observations.

SECTION 3
EXPERIMENTAL SET-UP

This chapter is divided into two main subsections. The first describes the physical apparatus that were used during the course of this experiment which includes the main discharge system, a review of the electrode systems, the plasma opening switch, the aluminum preconditioner, and the fiber loader. This is followed by a discussion of the relevant diagnostics used to perform measurement on the exploded aluminum wires or carbon fibers.

3.1 PULSED POWER SYSTEM.

The exploding wire pulsed power system used in this experiment will be described in the following sections which include the discharge system, the low energy preconditioning circuit, various electrode systems, the plasma opening switch (POS) and the fiber loader. Although the system was designed to explode single and double wire loads, frequently references to a "shorted" load are made. This load usually consisted of a 0.75 inch diameter bar which was inserted in place of the wire load. It was used to check the electrical performance of the system and calibrate current monitors since, in contrast to a wire load, the inductance was constant in time.

3.1.1 Parallel Plate Discharge System.

The discharge system that was used for this experiment was similar to a system that had been in operation at the University of California at Irvine.[23] The basic discharge system, except for electrode modifications, remained essentially unchanged during the course of the experiment. A schematic drawing of this facility is shown in Figure 3-1. A set of four 1.85 μF Scyllac capacitors were connected in parallel by a triplate transmission line and switched into a coaxial electrode system by a Maxwell model 40200 rail gap switch. The capacitor bank operates with voltages up to 50kV. A seven stage 140 kV mini-Marx bank built according to the design developed at Los Alamos National Laboratories triggered the rail gap switch producing multi-gap breakdowns in the switch. HY-Tech incorporated a Krytron switched capacitive discharge circuit to trigger the mini-Marx. The trigger sequence was initiated by
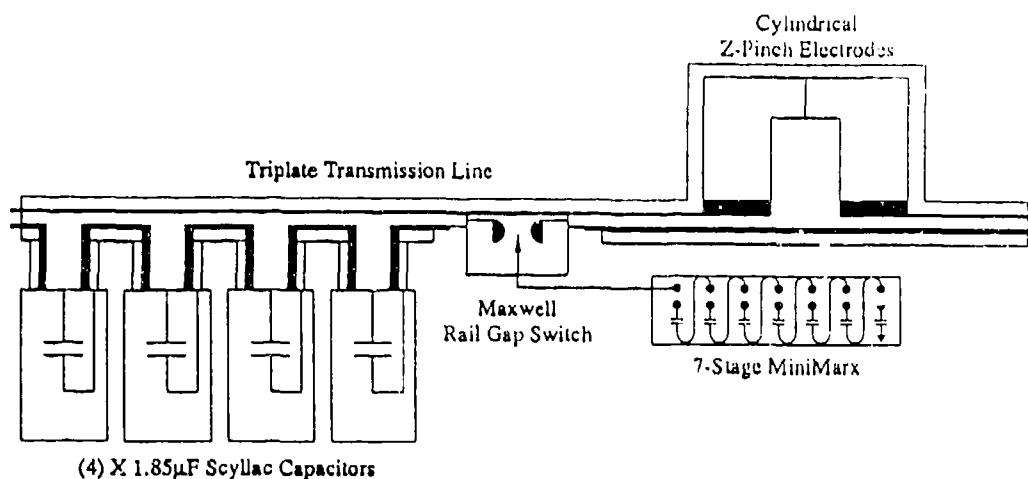
Figure 3-1. The z-pinch pulse power system showing the triplate transmission line, rail gap switch, and generic coaxial z-pinch electrodes.

a 350 volt pulse from the control console.

3.1.2 Aluminum Preconditioning Circuit.

Concerns over the incomplete vaporization and subsequent ionization of the aluminum load material led to the development of a low energy preconditioning circuit. The circuit drove an axial current through the aluminum load. By doing so, the preconditioner attempted to uniformly heat the load through its solid and liquid phases to boiling. At that point, the z-pinch discharge system was switched across the preconditioned load.

The preconditioning circuit is shown in Figure 3-2. Four 2.7 nF 40 kV capacitors were connected to form a 2.7 nF 80 kV bank. The 80 kV capability was built into this circuit so that when used in conjunction with the z-pinch discharge, it could absorb large inductive voltages associated with pinching. The preconditioner bank was charged to 15 - 40 kV and switched with a PT-55 triggered spark gap switch. The oscillation period for a discharge through a 0.75 inch diameter short circuit was 315 ns, implying a system inductance of 930 nH. The inductance with an aluminum load was near 1 μH.

The current and voltage waveforms obtained with a 20 kV charge and an 8.5 mm long aluminum load are shown in Figure 3-3. The current rose to a peak of 600 A and the voltage to 6 kV in less than 100 ns. After peaking, the voltage abruptly dropped implying the onset of ionization in the load region.

15
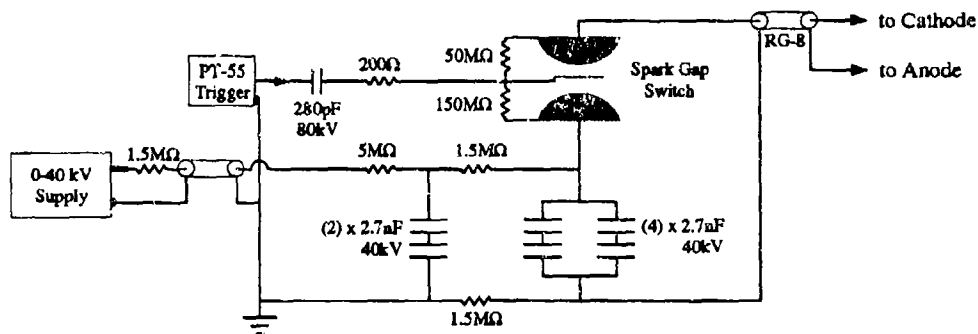
Figure 3-2. Low energy preconditioner circuit for vaporizing aluminum loads.
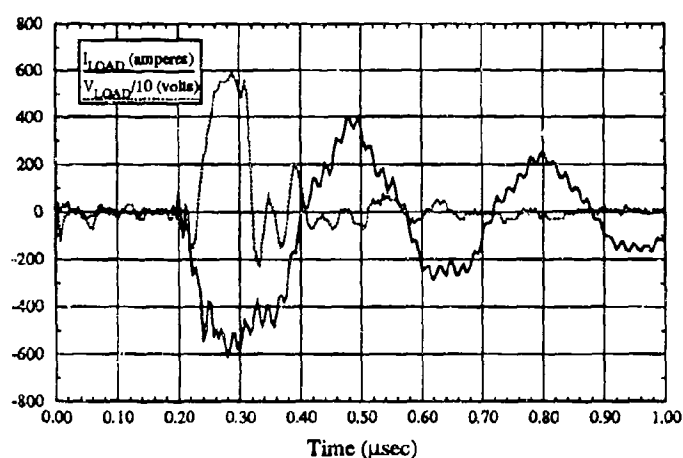
Figure 3-3. The current and voltage waveforms obtained with the preconditioner charged to 20 kV and using an 8.5 mm long aluminum load.

3.1.3 Electrode Configurations.

The coaxial electrodes and interface have been modified several times throughout the course of this program. There were four distinct electrode/interface configurations, Electrodes I-IV, that were used during this experiment. The first two were constructed to explode wire loads by a direct discharge of the capacitor bank, while the last two were designed to facilitate plasma opening switch operation. The sequence of electrode systems will be described chronologically.

The initial design was relatively simple, it contained a 45° insulator and is shown in Figure 3-4(a). The advantage of this design was its very low inductance. The current rise time of the system with a shorting bar inserted in place of the load was only 1 μs. This

16

corresponds to a total inductance of only 55 nH. This circuit produced 225 kA for a 20 kV charge which extrapolates to over 500 kA at full voltage. With a 2 cm length wire load, the inductance increased by about 30 nH and currents of 185 kA were obtained with a 20 kV charge.

(a) Electrode I   (b) Electrode II
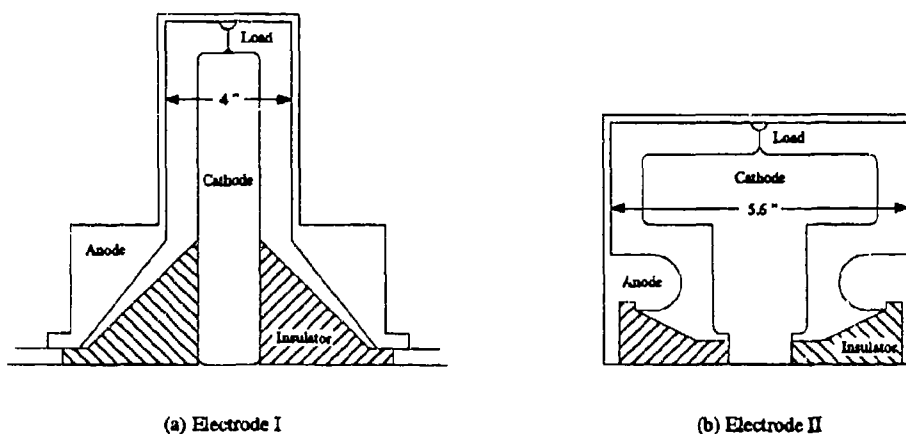
Figure 3-4. Electrode systems I and II used with a direct capacitive discharge.

Although the electrode system shown in Figure 3-4(a) was low inductance, unacceptable breakdowns across the interface, even at low voltage, forced us to redesign the top end. Initially, a number of simple modifications were tried. These included changing the shape of the existing interface, inserting a flat disk insulator in place of the angled one, and shielding the interface from load initiated UV radiation. When these proved unsuccessful, a new system, Electrode II, was placed on the machine. The redesigned system, shown in Figure 3-4(b), reduced the electric field strength at the triple points by appropriate shaping of the electrodes and provided better isolation of the interface from load initiated UV radiation. However, as a result there was an increase in the inductance to about 82 nH with a short, and the current rise time increased to 1.25 μs. Therefore, for a short circuit load Electrode II delivered 470 kA at full charge and 400 kA into a single wire. The breakdown problem which had been observed with the previous design was reduced significantly.

Motivated by the desire to investigate the effects of current rise times, it was decided that a POS would be inserted on the machine which would require a redesign of the electrodes. The POS would allow us to vary the current rise time by about an order of magnitude. The switch would be required to conduct for about a microsecond and, since this is a relatively long conduction time POS, $J \times B$ motion of the switch plasma toward the load was anticipated. Therefore, the new design called for an elongated electrode system so plasma

17

disruption of load operation would not be a problem. The result was the Electrode III design shown in Figure 3-5(a), which was tried using an array of 12 carbon plasma guns as a plasma source. Some of the parts from the previous design, including the interface, were used. There were a number of problems associated with this set up. The POS would only switch 60 kA to the load, and the interface was not very well isolated from the switch plasma. This performance was unacceptable, therefore a decision was made to use a flashboard driven plasma source for the POS and to improve the isolation of the interface.

(a) Electrode III   (b) Electrode IV
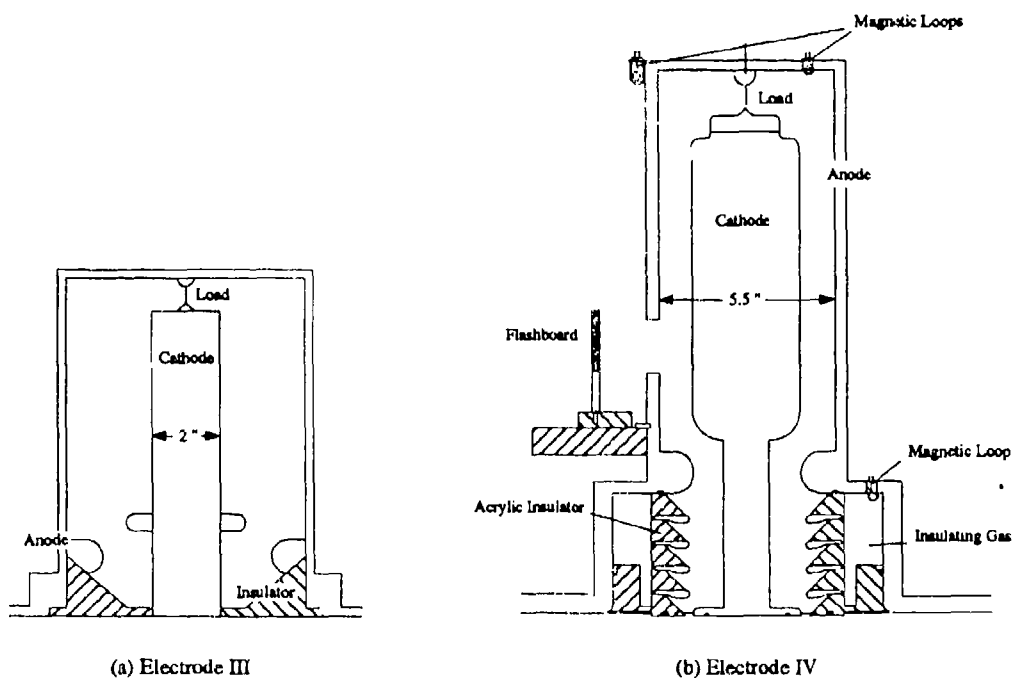
Figure 3-5. Electrode systems III and IV used with a plasma opening switch.

The final electrode design, Electrode IV, is shown in Figure 3-5(b). Essentially all of the data reported herein was obtain with this electrode system installed on the machine. It showed an improvement in breakdown characteristics compared to previous designs and provided enough isolation to operate a 6 flashboard plasma source for the POS. This system was designed with more stringent voltage hold-off requirements and better isolation from load radiation. The concern in this area had been breakdowns across the interface which could be due to electric field enhancements on the interface surface, or breakdowns initiated by UV radiation. The final design addressed both these issues. Two factors in the anode-cathode geometry led to an improvement in the isolation of the interface from load UV

18

radiation. A decrease in the anode radius and the addition of lobed structures increased the required number of reflection for load initiated UV radiation to strike the interface. The interface itself had been carefully designed by using an electrostatic field plotting code to minimize the peak electric field on the acrylic surface. The interface consisted of a series of acrylic rings, separated by conducting rings, which under an ideal situation grades the field so the electric potential across any two adjacent rings is about equal. Although the inductance was 25 nH less than Electrode III, it was still significantly larger than either of the first two designs. This was primarily due to the elongation of the electrodes. The system inductance with a 0.75 inch diameter shorting bar was 140 nH which resulted in a current rise time of 1.6 μs and a peak current of 365 kA at full charge. With a 25 μm diameter load, these numbers changed to 185 nH, 1.85 μs and 315 kA, respectively. The current rise times changed dramatically when the POS was operated, as will be explained in the next section.

3.1.4 The Plasma Opening Switch.

To achieve faster current rise times in the load, a plasma opening switch was installed on the coaxial feed line. The coaxial electrodes were extended axially in designs III & IV to provide a 20-25 cm conduction region between the switch and the load. In Electrode IV, the anode radius was also reduced, and a double-lobe configuration was used to protect a vertical stack interface from UV and plasma originating at the switch.

(a) Current Waveforms   (b) Conduction Time vs. Bank Voltage
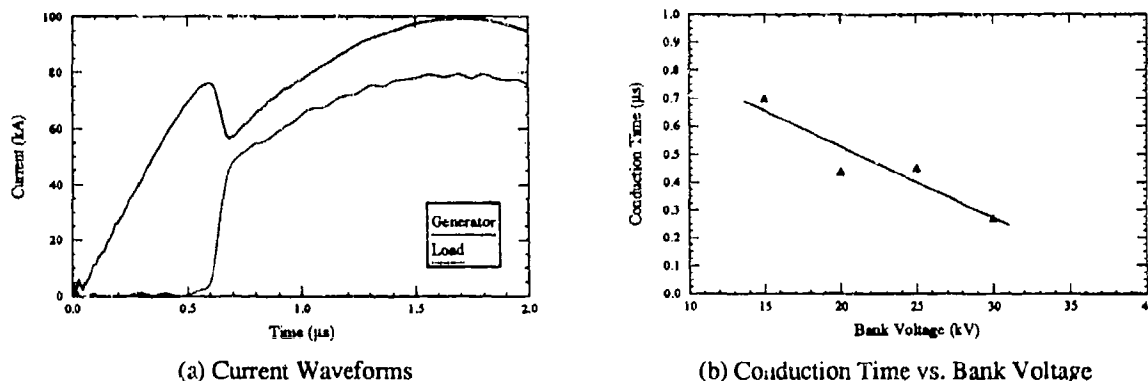
Figure 3-6. POS results using the 12 carbon plasma gun array. Machine and load current waveforms are shown in part (a) and a plot of conduction time versus capacitor bank voltage for four shots in (b).

Two different plasma sources were used for the switch. First, twelve carbon plasma guns,

or Mendel guns, directed plasma at the cathode through windows in the anode. The Mendel guns were fabricated by terminating the ends of 0.141-semirigid coaxial cable and feeding them through the vacuum chamber wall. All twelve guns were energized by a single 7.1 μF capacitor. The impedance of each gun circuit was measured to be 125 nH which implied that a 25 kV discharge produced approximately 15 kA of current in each gun rising in 1.5 μs. An open shutter camera verified that all twelve guns were producing plasma.

The performance of the opening switch using plasma guns was tested with a 3 cm diameter rod to act as a short circuit load. A current transformer placed around the rod was used to measure the load current, and a magnetic pick-up coil was used to monitor the generator current prior to the opening switch. Typical waveforms for the load and generator currents are shown in Figure 3-6(a). Average opening times were ~125 nsec, but the maximum switched current was only 50 to 60 kA which was unaffected by the main bank voltage. As the main bank charging voltage was increased, the conduction time decreased. This observation is summarized in Figure 3-6(b) which shows that for a 30 kV charge the conduction time was only $\approx$300 ns. The switch performance was unaffected by the gun voltage which was varied from 20 to 30 kV indicating that the injected density did not change. Various delay times, that is the time between firing the gun bank and the main bank, were also tried with no improvement in the switching current.
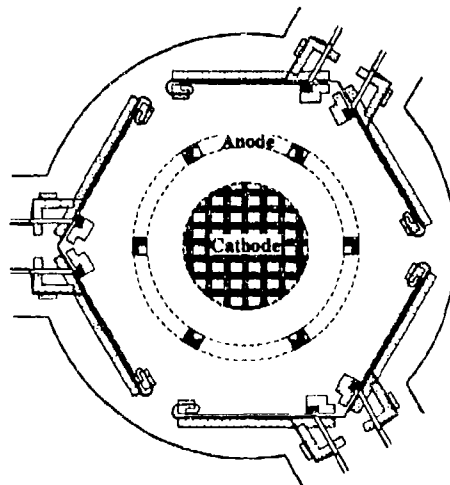
Figure 3-7. The plasma injection scheme using a six board array on the Electrode IV system.

These observations are best described by the following scenario. The switch opens when the current reaches about 50 kA. Longer conduction times are observed for the lower bank

voltages because it takes longer for the current to rise to the 50 kA level. At higher bank voltages very short conduction times were observed in accordance with the 50 kA limit. It was concluded that to conduct larger currents in the switch a plasma source capable of injecting much more plasma was needed.

(a) Driving Circuit

(b) Row Current vs. Time
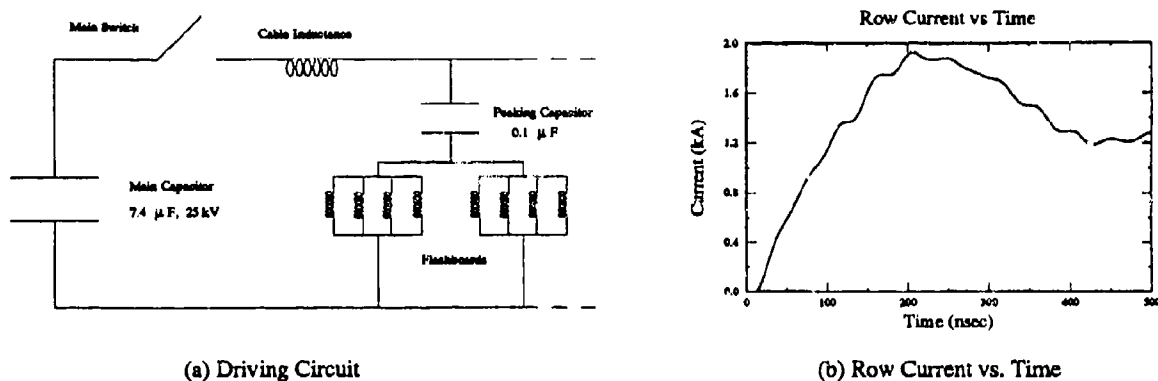
Figure 3-8. The driving circuit (a) and the measured current per row (b) for the flashboard plasma source.

To improve the performance of the switch an arrangement of six, four-row flashboards was used to inject plasma into the anode-cathode gap as shown in Figure 3-7 using Electrode IV. Each flashboard row contains sixteen 1.5 mm gaps coated with colloidal carbon. The same 7.1 μF capacitor and spark gap switch used for the Mendel guns was used as the main storage capacitor in this discharge system. However, three intermediate 0.1 μF capacitors pulse charged by the 7.1 μF capacitor act to sharpen the current rise to each flashboard. Each of the 0.1 μF capacitors is connected to eight rows (two flashboards) by eight, 20 cm lengths of RG-58 cable. The equivalent circuit for this arrangement is shown in Figure 3-8(a) where each row is represented as an inductive component. The circuit can deliver approximately 2 kA per row in 200 ns as shown in Figure 3-8(b). The flashboards were placed axially 22.5 cm from the load and radially 4 cm from the outside edge of the anode cage. To facilitate plasma injection, six windows were cut in the anode opposite the flashboards with each window 6.2 by 4.5 cm.

Approximately 100 shots were taken on the system with a shorted load to investigate the switch parameters at various machine voltages ranging from 20 to 45 kV. To control the amount of plasma injected into the A-K gap, the flashboard delay time was varied. This is the time between the arrival of current to the flashboards and generator current to the switch plasma. Of particular interest were the measurements of the switch opening time,

21
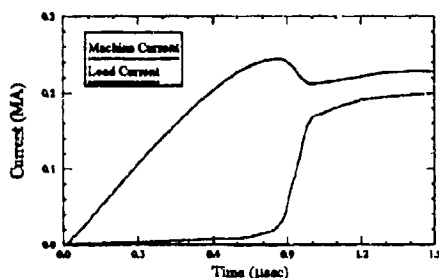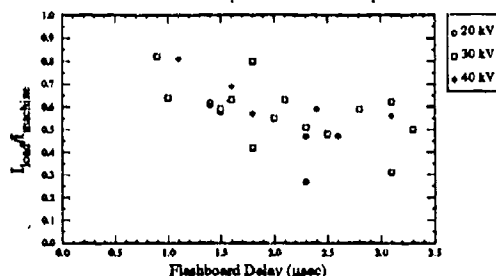
(a) Load and Generator Currents   (b) Efficiency vs. Flashboard Delay

Figure 3-9. The performance of the flashboard driven POS for (a), a single shot at 45 kV, and (b) the current transfer effeciency vs. the flashboard delay.

conduction time, the machine current when the switch begins to open and the ratio of load to machine current after opening. To make these measurements magnetic pickup loops were used to determine the load and machine currents, the locations of these loops are indicated in Figure 3-5(b). An example of the current probe readings for a shorted load is shown in Figure 3-9(a); in this case the machine was charged to 45 kV and the flashboard delay time was 3.06 μs. The measured conduction time was 0.82 μs, the opening time was 140 ns and 165 kA was switched to the load. The current transfer efficiency (I_{load}/I_{mach}) was 0.77 and the average value of dI/dt delivered to the short was 1.1 MA/μs. It was found that flashboard delays near 2.5 μs would produce similar results at 45 kV with shorter delays necessary at lower voltages down to 1.5 μs at 20 kV. A summary of the current efficiencies measured on a number of shots is shown in Figure 3-9(b). This shows that the best efficiencies were obtained for delays less than 2 μs with the average efficiency around 60%.

3.1.5   The Fiber Loader.

A fiber loader was used to reload fibers without breaking vacuum between shots. The original design was similar to that of Kania.[24] In this scheme, a long fiber is attached to a pushrod with silver paint. The rod and fiber slide through a quartz tube which directs the fiber through a hole in the center of the anode to the center of the cathode. A sliding O-ring seal on the pushrod maintains vacuum in the system. A positive DC bias applied to the cathode guides the fiber to the pointed cathode. When the fiber contacts the cathode, a capacitor in parallel with the power supply welds the fiber to the cathode. This action was successfully used for aluminum, carbon, and nickel fibers.

A new fiber is loaded after the preceding fiber has been exploded by simply depressing the pushrod further to feed a fresh segment of the fiber into the A-K gap. In this manner several shots, the number determined by the length of the fiber on the pushrod and the length of the A-K gap, can be taken in quick succession without breaking the vacuum.

This design has undergone several modifications to reduce downtime due to fiber loading. The original design resulted in complications when shots were taken with bank voltages exceeding 35 kV. The higher voltage shots caused the fiber to break off in the quartz guide tube, necessitating frequent, time-consuming removal and cleaning of the loader. This problem was remedied by employing an "air lock" which allowed vacuum in a very small volume to be broken and evacuated quickly. In this scheme, the pushrod is removed and a new length of fiber is attached for each shot. The air lock acts as an intermediate step between atmospheric pressure and the vacuum system so that the pushrod and fiber can be quickly removed and installed with virtually no pumping time necessary. This mechanism has resulted in a system that can be reloaded and ready for a shot in several minutes.

3.2 DIAGNOSTICS.

This section, covering the diagnostic measurement techniques that were employed during this experiment, is organized in the following manner. A brief discussion is presented of the equipment and/or apparatus that were common to a variety of the diagnostics. The remainder of the section contains discussions of specific diagnostic techniques and is organized into a subsection on imaging diagnostics, one on spectral diagnostics, and another on miscellaneous diagnostics.

3.2.1 Equipment.

Various pulsed lasers were used for many of the imaging diagnostic techniques. A Continuum model 580-30 Nd:YAG laser was used for most of the double exposure holographic interferometry and for obtaining framed shadowgrams. This laser had a nominal pulse width of 9 ns and maximum power of 200 mJ. For the measurements we performed, a frequency doubling crystal was used to reduce the wavelength to 5320 Å, where holographic film was readily available. Holographic film with AGFA 10E75 emulsion, at 3000 lines/mm, was used exclusively. The laser energy level at this wavelength was approximately 50 mJ yielding an average power of about 6 MW. During the early stages of the experiment, holographic recordings were made using a Korad K-1 pulsed ruby laser. This laser, at 6943 Å and 40 ns, had a somewhat longer wavelength and pulse width then the frequency doubled YAG. However, average power outputs were in the same range as the YAG laser. A Phase-R, model

23

2100 pulsed dye laser was also used for making framed interferograms, but, its relatively long pulse width made it more suitable for the backlighting of streaked shadowgrams or absorptiongrams. It was typically operated at a wavelength of 5850 Å and a pulse width which could be 250 or 500 ns.

A valuable piece of equipment which allowed us to perform interferometric measurements with the long pulsed dye laser and streaked shadow/absorptiongrams, was a Kentech model OSC12 image intensified streak/framing camera. The streak and or frame duration on this camera could be set between 20 ns and 3 ms at manufacturers defined intervals. Typically streak duration times were 300 ns or 1 μs, and frame speeds of 20 ns were used for the interferometry.
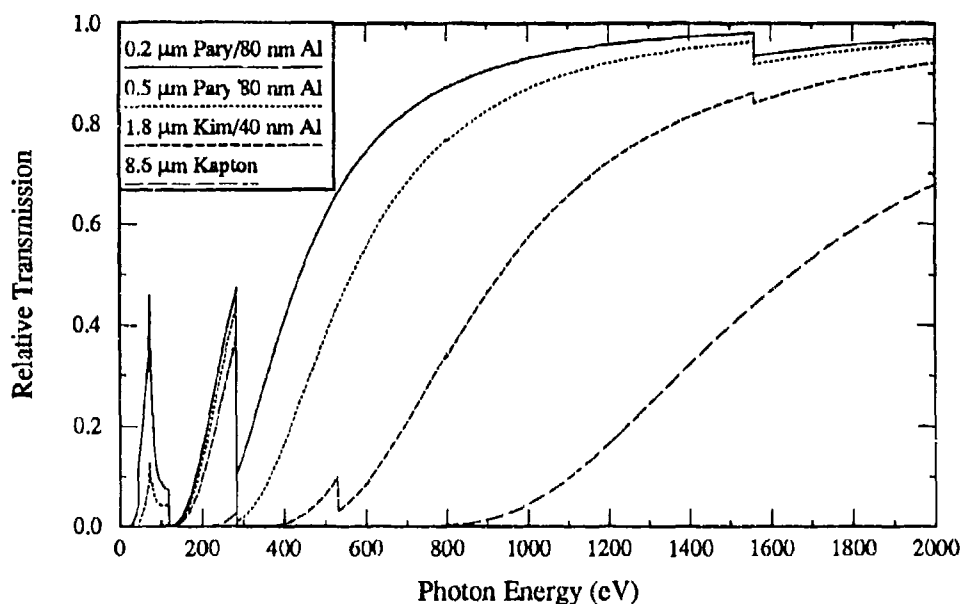
Figure 3-10. A plot of the relative transmission as a function of photon energy for single layers of 0.2 μm Parylene, 0.5 μm Parylene, 1.8 μm Kimfoil, and 8.6 μm Kapton.

The implementation of x-ray imaging diagnostics used in this experiment, as well as time resolved measurements with x-ray diodes, required the use of filters which prevented visible light from being detected while letting the x-ray radiation through. For this purpose we used Parylene filters, with thicknesses of 0.2 or 0.5 μm, that were coated with 800 Å of aluminum.

24

The aluminum coating was sufficient to block the visible light and the Parylene, which is a hydrocarbon, let through relatively low energy x-rays. Additional filters were used for energy discrimination of the emitted radiation. The higher energy x-ray filters used were 1.8 μm Kimfoils with 400 Å of aluminum and 8.6 μm Kapton. These filters were normally used in conjunction with the Parylene filters. Figure 3-10, shows the relative transmission through single layers of the two types of Parylene, Kimfoil, and Kapton filters. Generally this plot shows that transmission through a single Kapton filter effectively measures radiation above $\sim$1.5 keV. Single filters of Kimfoil, 0.5 μm Parylene, and 0.2 μm Parylene allow progressively lower energy x-rays to reach the detector. In addition, both Parylene filters and the Kimfoil transmit in a band around 200 to 300 eV where the Kapton does not. The transmission through combinations of these detectors is obtained by multiplying the appropriate response curves to come up with a net filter function.

3.2.2   Imaging Diagnostics.

The imaging diagnostics that were employed will be described in this section. These techniques are subdivided into five categories and include methods which use visible and x-ray plasma emission as well as lasers for the formation of holograms and backlighting.

Open Shutter Camera

Our open shutter view camera diagnostic, which was employed on many shots, consisted of a camera loaded with Polaroid film that was focused on the load region. Before a shot, the shutter was opened manually. It was then closed after the shot. Typically neutral density filters were required to obtain an image that was not overexposed, the nd range was 2.0. These photos give use the time integrated optical emission from the load.

X-ray Pinhole Camera

This camera is the x-ray counterpart to the open shutter view camera. It was operated in an identical manner; the only major difference between the two devices was that we used a pinhole, most often 30 μm in diameter, to image the load onto the film directly. The photos obtained from this camera give us the time integrated x-ray emission through various filter arrangements. Most often this diagnostic was used as a monitor and 0.5 μm Parylene filters were place directly in front of the pinhole. The camera was typically loaded with Kodak DEF x-ray film.

25

3.2.3 Gated Microchannel Plate Framing Camera.

This camera, a Pulsed Imaging Products model GMPFC-1, was used to image x-radiation from the load. It was commonly referred to as the "PIP", and detailed descriptions of its operation have been published.[25] The device contained seven independent striplines which are sensitive to x-radiation and are activated by applying a voltage in the 8 kV range. An array of seven pinholes was aligned with the striplines so each stripline saw the load through one pinhole thus minimizing crosstalk. Filters were placed in front of the pinhole array to remove visible light and discriminate the x-radiation. The diameter of each pinhole was 50 μm. The width of the voltage pulse to each stripline determined the framing speed, which could be less than a nanosecond, and the arrival of the voltage pulse determined its timing. The actual control of the voltage pulse width, as well as the arrival of the voltage pulse at the stripline, were set by varying the length of the appropriate transmission line. In practice this meant changing the physical length of RG-58 cables. Due to dispersion and attenuation in the cable an upper limit on delay times was 50 ns between striplines, or about 33 feet of cable.

The two most common arrangements when using the PIP were sequential gating of striplines to obtain a seven frame time history of the x-ray emission, and simultaneous gating of striplines with a differential filtering scheme for the pinholes. An example of a sequential gating scheme would be to set the frame duration for each stripline at 10 ns and set the delay between adjacent striplines at 25 ns. Therefore, in this case, the seven picture sequence would span a total of 220 ns. Simultaneous gating simply means that all the striplines come on at the same time for the same duration. This is particularly useful if the pinholes contain different types of filters. In those cases we determined where the low and high energy x-rays were emitted on a particular shot at a particular time.

Interferometry

In most cases interferometric measurements were performed on the plasma by creating double exposure holograms with the YAG or ruby lasers. These lasers were set up in a Mach-Zehnder arrangement as shown in Figure 3-11. These techniques for plasmas have become a standard diagnostic tool.[26] Additional interferometric measurements were also made with a dye laser in a conventional Mach-Zehnder arrangement. The dye laser arrangement is also shown in Figure 3-11.

The interferometric analysis requires that two holograms be exposed on the same piece of film. One of the holograms contains the phase distortion due to the plasma plus that due to the optical components, this is analogous to the scene arm of a conventional interferom-
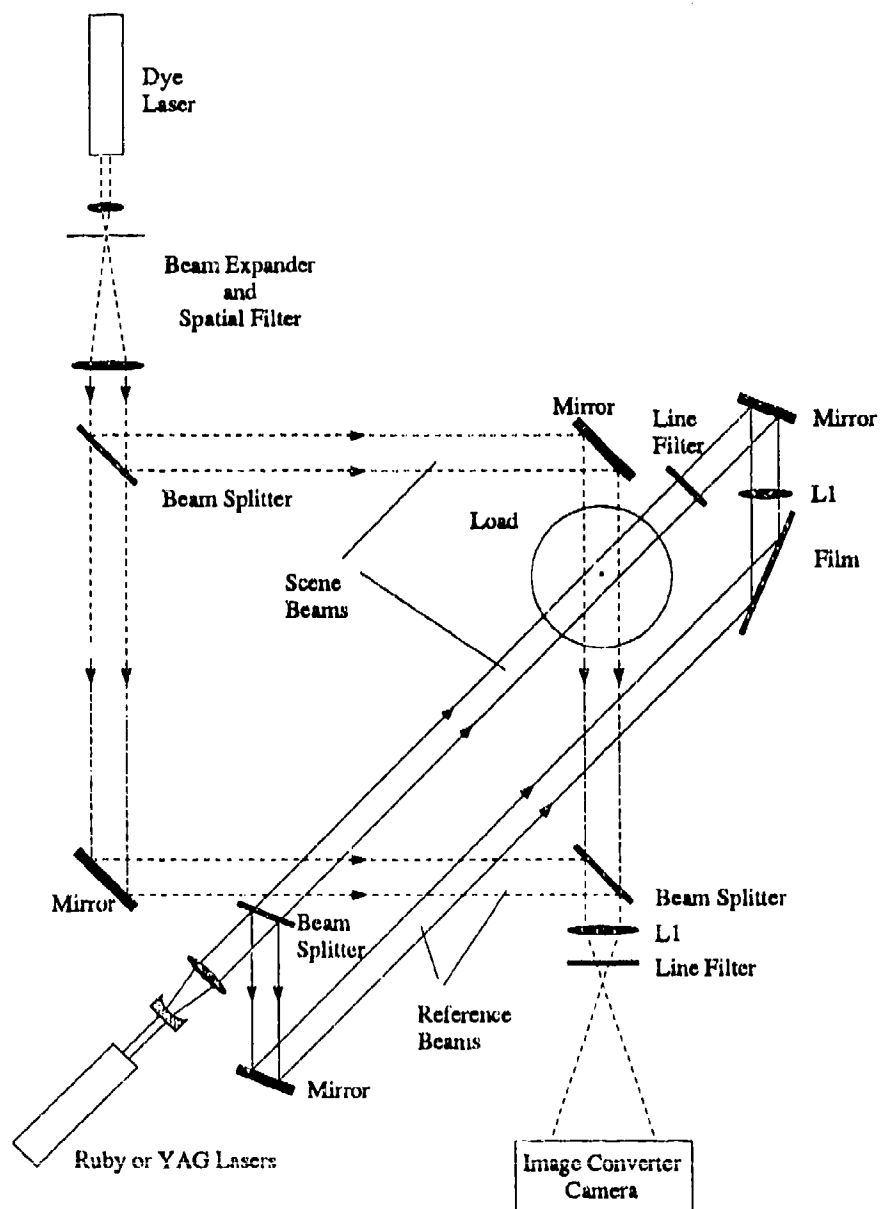
Figure 3-11. Schematic experimental arrangements of optical components for the dye laser interferometer and the holography system using the ruby or YAG lasers. The lens L1 in either configuration corrects for plasma refractive effects.

eter. The other exposure is simply taken with plasma absent, which is the analogue to the reference arm, and it contains only the phase distortion due to the optical components of the holographic system. During reconstruction the two images interfere with one another and a fringe pattern is observed. The fringe pattern is interpreted in the same fashion as in conventional interferometry. Assuming that the optical components do not move between exposures, the fringe pattern in double exposure holography is due only to the phase distortion introduced by the plasma since the optical component distortion is present on both exposures. Typically a small angular difference in the reference beam is introduced between exposures so a pattern of straight line background fringes is observed without the presence of plasma. It is the distortion of the background fringe pattern which can be related the the index of refraction of the plasma, and ultimately the plasma electron density.

A conventional Mach-Zehnder interferometer was also used with the dye laser. For this set up, higher grade optical components were required since the observed fringe pattern will reflect distortions of these components. Due to the long pulse width of the dye laser, 250 ns, the interference pattern was recorded through a 20 ns framing camera. If an open shutter camera was used, dynamic changes in the plasma during the 250 ns pulse width would smear the interference pattern. Therefore, with our set up, the scene and reference beams were set to interfere at the last beam splitter and this pattern was imaged with a lens onto the Kentech camera. The output from the camera was recorded directly on film.

The analysis of interferograms of this type is standard practice and details are available from many sources.[27] A relationship between the fringe distortion on the interferogram and the line integrated electron density is obtained as follows. The plasma electrons increase the phase velocity of the laser light, V_{ph}, according to

$$V_{ph} = \frac{c}{[1 - \omega_p^2/\omega_o^2]^{1/2}} , \tag{3.1}$$

where c is the velocity of light, ω_o is the laser frequency, and ω_p is the plasma frequency which depends on the plasma density. The accumulated phase difference due to the plasma will be

$$\Psi = \int \left(\frac{\omega_o}{V_{ph}(z)} - \frac{\omega_o}{c} \right) dz , \tag{3.2}$$

where the integral is taken over the path of the laser through the plasma. One fringe shift will correspond to an accumulated phase difference of 2π. Considering only effects due to electrons, which is a very good approximation, the above integral can be solved to yield the line integrated electron density required for one shift,

$$\int n_e(z)dz = \frac{m_e c \omega_o}{e^2} = 3.2 \times 10^{17} \text{ electrons/cm}^2 , \tag{3.3}$$

28

where the above result was obtained using the ruby laser frequency. The corresponding numbers for the YAG and dye laser frequencies are 4.2×10^{17} and 3.8×10^{17} electrons/cm^2 respectively.

It should be pointed out that the holographic set up shown in Figure 3-11 has a lens, L1, which is adjusted to focus the plasma onto the film. The purpose of this lens is to correct for the refractive bending of the laser light by the plasma. If collimated light is used and refractive bending was absent, there would be a correspondence between the position of a light ray on the film and its position in the plasma. This correspondence is necessary so the interferometric information can be inverted and the electron density as a function of position determined. Since the plasma is essentially a defocusing element, light rays are bent from there normal trajectories and the lens is required to restore correspondence between film position and position in the plasma.

Due to the fact that the plasma has cylindrical symmetry and the laser path is perpendicular to the z-axis of the pinch, the information obtained from the interferograms must be Abel inverted to obtain the electron density as a function of the radial coordinate r.[28] Examples of the results from these inversions will be shown in latter sections.

Absorptiongrams and Shadowgrams

Both streaked and framed absorption/shadowgrams were routinely made of various types of plasma discharges. Two distinct modes of operation were used, streaked and framed. The framed mode is conceptually very simple. These were created using the pulsed ruby or YAG laser by either taking a single exposure hologram or removing the reference arm from a double exposure hologram. The streaked mode required the use of the longer pulsed dye laser and the Kentech camera.

Examples of framed absorptiongrams will be shown in later sections. Essentially a 2-D picture of the plasma is taken with a short pulsed laser, either the ruby or YAG. The holographic experimental set up was used to create these pictures. Since the refractive effects of the plasma are corrected for by the imaging lens as explained in the previous section, the absorption effects are recorded. A single exposure hologram will accomplish this and many of these were taken. But, it was possible to obtain the same information from a double exposure hologram and block out the second exposure during reconstruction. The procedure for this was the following. Upon reconstruction, the virtual image contracts to a very small spot and then expands as the observer moves away from the hologram plane. Provided that the angle between exposures during construction was large enough, the spot can actually be resolved into two spots with each spot corresponding to one of the exposures. The no plasma

exposure can be removed simply by placing a knife edge at the focus of the appropriate spot thus blocking this image and preventing the two from interfering. Therefore, the expanded image after the knife edge is the single exposure hologram of the plasma.
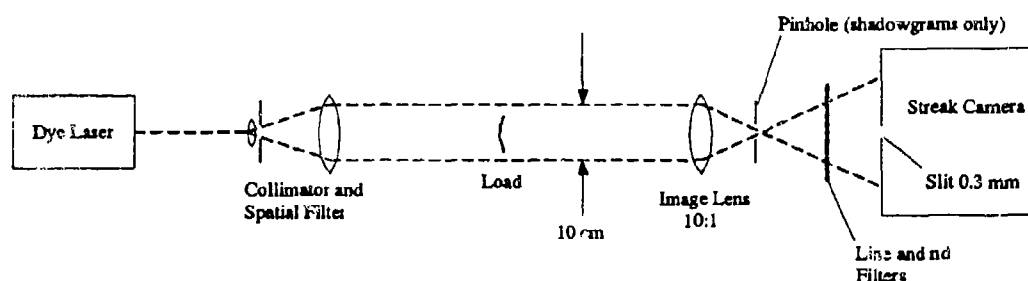
Figure 3-12. Experimental arrangement of optical components used to take streaked absorptiongrams or shadowgrams.

When using the streak camera and the dye laser for backlighting both absorptiongrams and shadowgrams were taken. The experimental set up for this is shown in Figure 3-12. The information obtained from the streaked absorptiongram is the same as that from the framed absorptiongram except one spatial dimension is replaced by time. With the slit shown in Figure 3-12 oriented perpendicular the z-axis of the pinch, the streak gives us the absorbing radius as a function of time. Of course the direction of time is also perpendicular to the slit.

A shadowgram is obtained by inserting a pinhole into the set up as shown in Figure 3-12. This effectively removes some of the refracted rays from the laser beam which would normally be captured by the lens and recorded. Thus, we can introduce a shadowing effect to varying degrees by changing the size of the said pinhole. Pinhole sizes ranged from 2 to 8 mm. Off course with this set up absorption and/or emission effects would still be present. It should be noted that a shadowgram could also be obtained by removing the lens completely since collimated light was used. However, when that was tried the refractive effects were so overwhelming that the streaks were essentially unintelligible. Many examples of streaks will be shown in later sections.

3.2.4   Spectral Diagnostics.

By spectral diagnostics we essentially mean measurements which shed light on the spectral distribution of emission from the plasma. Crudely speaking, filtered x-ray diodes and

photoconducting diodes fall into this category as well as visible light spectroscopic measurements that were performed on the preconditioned plasmas.

Photoconducting Diodes

The time resolved x-ray emission from the plasma was routinely measured with either photoconducting diodes (PCDs) or x-ray diodes. Detailed documentation on the operation and/or construction of these devices have been reported in the literature.[29, 30] The majority of our measurements used PCDs composed of intrinsic gallium arsenide or chromium-doped gallium arsenide (GAD). The advantage of these devices was their fast time response, relatively flat spectral response over a wide range of photon energies, and the fact that they essentially do not saturate which is a common problem with XRDs.
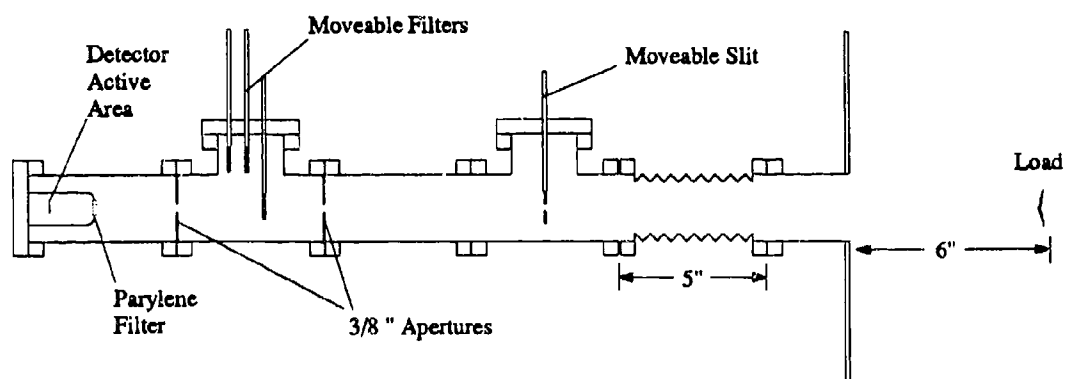
Figure 3-13. Set up of a photoconducting diode in the experiment. The combination of two 3/8" apertures and a slit assured that the detected signal was due to load radiation.

The physical set up of these devices is shown in Figure 3-13. The detector was mounted inside a N-type connector which was fed directly into the vacuum system. Great care was taken to assure that the detected signals were coming from load radiation. Therefore, as illustrated in Figure 3-13, each PCD was mounted on extension tubes that contained a series of baffles and an aperture directly aligned with the PCD and the load. The aperture assured us that the direct line of sight contained only the load region and not the electrodes near the load. The aperture size as well as its position could be varied so as to view varying lengths or sections of the load. The baffle system was put into place to guard against small angle reflections of the electrode radiation which could make it to the detector. As many

31

as three individual detector stems could be mounted on the system simultaneously although routinely only one was monitored.

The filter arrangement system could also be varied. Typically a 0.2 or 0.5 μm Parylene filter was always mounted directly in front the the PCD or XRD on the N-type connector. Additionally, at some point downstream a series of flags with various filters mounted to them could be placed in the detector line of sight. This set up allowed us to vary the filter arrangement without opening the vacuum system.

Spectroscopic Diagnostics

Spectroscopic measurements of emission from the preconditioner discharge were made with a SPEX Model 1401 spectrometer used as a 0.75 m spectrometer. The light was collected from the load region which was then focused into a 400 μm diameter UV optical fiber. The fiber transmitted the light into the shielded room and illuminated the input slit of the spectrometer. A gated spectrum was obtained with an EG&G PAR Model 1456 optical multichannel analyzer (OMA). This detector was located in the output focal plane of the spectrometer. The detector gate duration ranged from 100 ns to 10 μs for pulsed shots and was continuous for calibration and focussing. The reciprocal dispersion in the wavelength range investigated was approximately 0.28 Å/pixel. Each pixel is 25 μm wide.

Time resolved measurements of line intensities were achieved using the same input optics and optical fiber to illuminate the input of a Heath 0.25 meter monochromator. A PMT placed at the output slit recorded the time history of the line for which the monochromator was set.

3.2.5 Miscellaneous Diagnostics.

Magnetic Pick Up Loops

Magnetic pickup loops were employed to measure the current flowing into load as well as the machine current. The outputs of these loops were recorded as raw signals and then integrated numerically to obtain the current as a function of time. They were all single turn loops which have very good frequency response with rise times in the nanosecond range.

Three main locations for these loops were typically employed as illustrated in Figure 3-5(b), which shows the Electrode IV system. The loop located near the acrylic insulator interface in the SF_6 insulating gas was referred to as the machine B-dot. The integrated signals from this loop indicate the current flowing past the interface and we commonly referred to this as the machine current. This loop was was attenuated by 20 dB into 50 Ω.

The signals from the two loops located near the top in Figure 3-5(b) reflect the current flowing into the load, there were also attenuated by 20 dB and terminated into 50 Ω. The loop located inside the return current cage could only be used reliably with short circuit loads where plasma was not formed. During aluminum wire load shots or carbon fiber shots, radiation and/or plasma disturbed the operation of this probe quite early into the current pulse. Therefore, for these types of loads the current was obtained using the probe located outside the return current cage. This loop was positioned behind a post adjacent to a view window which was used to observe the plasma. With this arrangement there was no direct line of sight from the pick up loop to the load. The signal is obtained from flux which escapes through the window and is picked up by the loop. This loop would give us a reliable reading for at least the rise time of the machine current.

The loops were calibrated against a T&M Research Products Inc. model CT6.5-685-5-100 current transformer with a sensitivity of 10 kA/volt. During the calibration shots the current transformer was placed in the system so that it would read the current flowing through a shorted load. All the probes were then calibrated against this signal.

Debris Collection

Debris ejected from the load region was collected on 0.5 inch square quartz substrates placed at various radial distances from the load. These substrates typically collected the debris from 5 to 20 successive shots.

The collectors were analyzed using a scanning electron microscope (SEM) to locate and determine the size and shape of collected particulates. Additionally, during SEM operation, x-ray fluorescence emitted from the sample was analyzed with an energy dispersive detector to determine the chemical composition of the particles.

SECTION 4
EXPERIMENTAL RESULTS

This chapter is divided into four main sections. Results from exploded carbon fibers, single aluminum wires, double aluminum wires, and arrays of layered magnesium on aluminum wires. The purpose of this chapter is not to analyze or draw conclusion about these measurements, however, it is meant as a presentation of the raw data which is a fair representation of a large quantity of measurements that were performed. The subject of analysis is left to discussion in the next chapter.

4.1 MEASUREMENTS OF EXPLODED CARBON FIBERS.

In this section we will describe the general features of the exploded carbon fibers that were used during the course of this project. A variety of fiber types were tried with diameters ranging from 10 to 33 μm and variations in resistivity from 14 to 2.5 $\mu\Omega$-cm. No significant differences were observed with our diagnostics from among these types of carbon fibers. Therefore, the figures included in this section pertain to 33 μm, 14 $\mu\Omega$-cm fibers simply because we have the largest data base using this type. However, the observations obtained with these loads, using our array of optical and x-ray diagnostics, differed drastically from those using aluminum wires, which will be reported in the next section. The carbon fibers showed the persistence of a solid, or very dense neutral core, surrounded by a corona type plasma that was apparently carrying the current. At lower machine voltages, our diagnostics clearly showed solid mass even though the machine current should have vaporized the carbon if it was flowing through the load. This lead us to conclude that the bulk of the carbon mass was never vaporized and that only a small fraction of the mass actually carried the machine current. Virtually every imaging diagnostic used during the course of this experiment corroborated this conclusion.

Most of the carbon load shots were taken with electrode systems II, III, and IV. No carbon fibers were exploded using the opening switch. The measurements obtained using these two electrode systems were essentially identical despite the differences in the current rise time and load length. For Electrode II the current rise time was 1.3 μs with a 2 cm length load and for Electrodes III and IV these numbers were 1.8 μs and 1 cm, respectively.

34
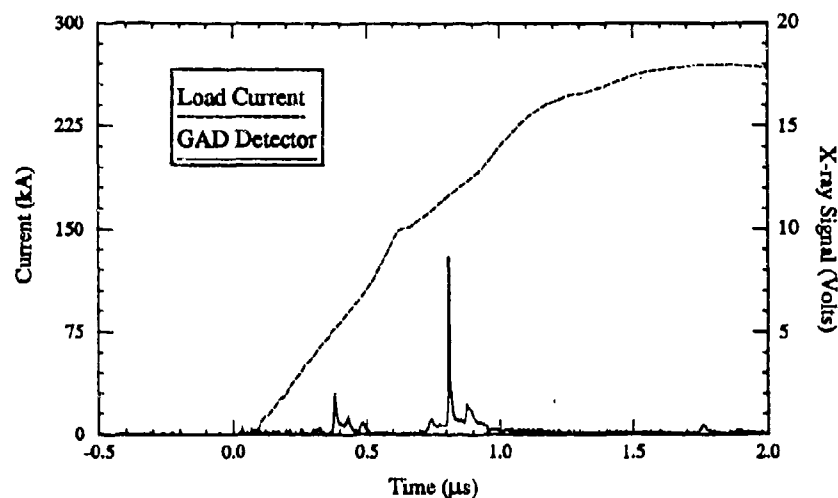
Figure 4-1. A signal obtained on a GAD detector with a 33 μm carbon fiber, the load current is also displayed. The shot used Electrode IV, the charging voltage was 40 kV, and the diode filter was a 0.2 μm Parylene foil coated with 800 Åof aluminum.

4.1.1   X-ray Measurements.

Time resolved x-ray measurements were routinely made using photoconducting diodes (PCD), x-ray diodes (XRD), and gallium-arsenide diodes (GAD). These served as a general monitor of the shot and to determine the type of radiation being emitted. When the GAD detectors became available they were used almost exclusively since they essentially do not saturate. Filters were typically employed to block optical radiation while allowing various ranges of soft and hard x-ray to be detected. An aperture system was also set up for these detectors so various axial lengths in the load region could be viewed. Two or three, usually GADs, were normally present on the machine for each shot. Generally, hard x-rays were emitted from the electrodes but not in the body of the load. This was determined by using a 10 μm aluminum filter to block everything but the harder radiation. With this filter, signals were observed on the detectors that viewed the electrodes but no signal was observed on those that viewed the load. The apertured detectors which viewed the load typically showed signals which exhibited a multiple peak structure. Filters used for these measurements were combinations of 0.2 & 0.5 μm Parylene, Kapton, and Kimfoils. Generally, it can be stated that as the number of filters increased the observed peaks became narrower in time and smaller in magnitude. A typical signal obtained with a GAD detector through a 0.2 μm

35

Parylene filter is shown in Figure 4-1. The observation of multiple peaks as displayed in the figure was common, however, the timings of these peaks were not consistent. Frequently, as in this case, the largest peak roughly occurs at the same time as the dip observed in the load current signal.

4.1.2 Observations with Imaging Dianostics.

The results from open shutter cameras, which are time integrating, are shown in Figure 4-2. These were both taken with 33 μm carbon fibers. Part (a), which is an x-ray pinhole camera, was taken through a 30 μm pinhole and a 0.5 μm Parylene filter using Electrode IV. For this shot the system was charged to 35 kV. The photo exhibits emission confined to a very narrow region for the bulk of the load with the brightest and broadest emission at the cathode tip. Close examination of this photo also shows a very thin black line through the center of the exposed area. In some of the more overexposed areas this line is masked out, but, a essentially continuous line is can be inferred. An open shutter optical camera result is shown in part (b) for a 25 kV shot using Electrode II, these pictures were taken with neutral density filters. The emission is confined to a very narrow region, in contrast to similar pictures taken with aluminum loads, with more significant emission at the cathode.
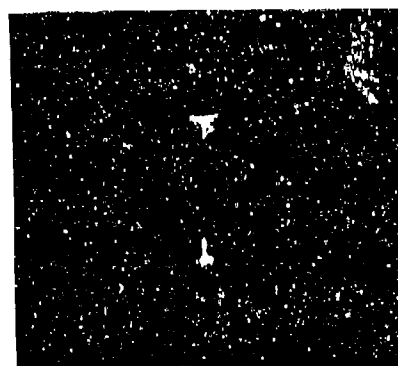
(a) x-ray camera   (b) optical camera

Figure 4-2. Photos of a 33 μm carbon fiber pinch with open shutter cameras for, (a), a 0.5 μm Parylene filter x-ray pinhole camera at 35 kV and, (b), a neutral density filtered optical camera at 25 kV.

Additional imaging diagnostics are shown in Figure 4-3. These photos are double exposure holographic interferograms taken with the short pulsed YAG laser. They were shot on separate 40 kV main bank discharges using Electrode IV. Parts (a), (b), and (c) correspond
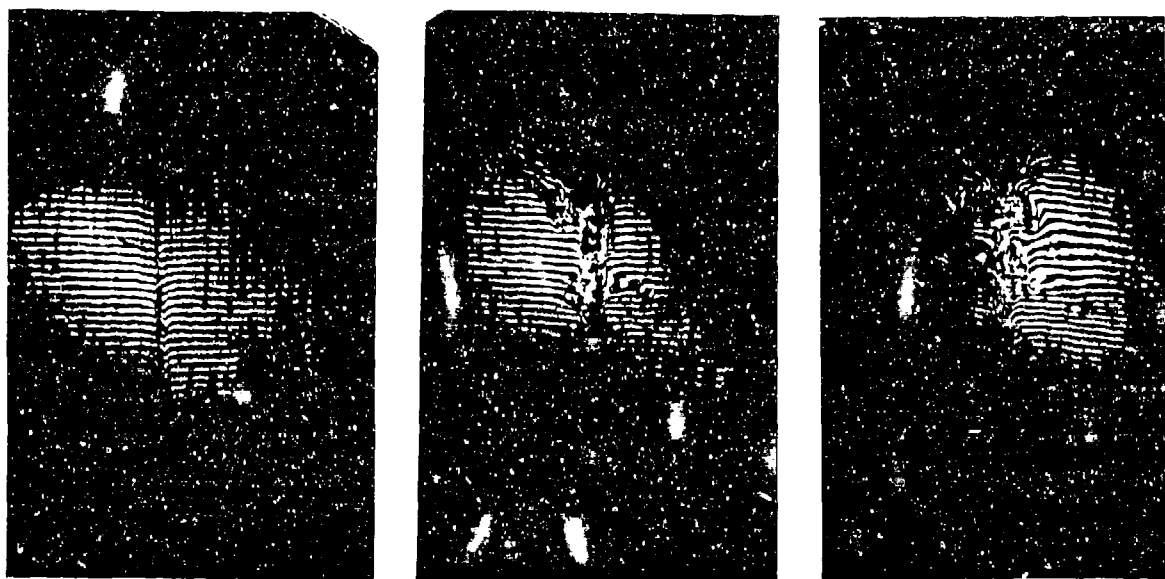
(a) 265 ns   (b) 350 ns   (c) 460 ns

Figure 4-3. Reconstructions of double exposure holograms using the short pulse YAG laser on 40 kV shots with 33 μm carbon fibers. Parts (a), (b), and (c) were taken 265, 350, and 460 ns after the start of current, respectively.
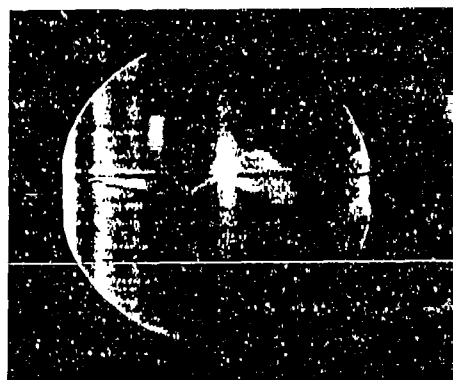
Figure 4-4. An example of a streaked shadowgram obtained with a 33 μm carbon fiber. The streak duration is 300 ns and it begins 275 ns into the current pulse. Time advances from left to right.

37

to exposures at 265, 350, and 460 ns into the current pulse, respectively. These pictures show a very well localized core where laser light has been blocked and the fringes cannot be followed through. The fringes are also very abruptly cut off indicating a very sharp density gradient of electrons. Using this diagnostic, it is very difficult to determine the status of the central region. We can say, however, where the plasma density begins.

Figure 4-4 is an example of a streaked shadowgram also obtained with a 33 μm carbon fiber. For this shot the main bank was charged to 30 kV using Electrode III. The streak duration was 300 ns and began 260 ns into the current pulse. There is therefore an overlap temporally with two of the holograms in Figure 4-3, although it is noted that the streaked shadowgram was taken with at a slightly lower charging voltage. The photo shown in Figure 4-4 is typical in that a significant expansion of the bulk fiber was never observed. This is in direct contrast to the aluminum load shots which are presented in the next section. The carbon shadowgrams do show "streamers", or thin refractive shells, which appear to expand radially or implode onto the fiber. This was observed on essentially all of the streaks, however, the occurrence of these streamers was completely random and sometimes not symmetric.

(a) before discharge   (b) 1.3 μs after discharge
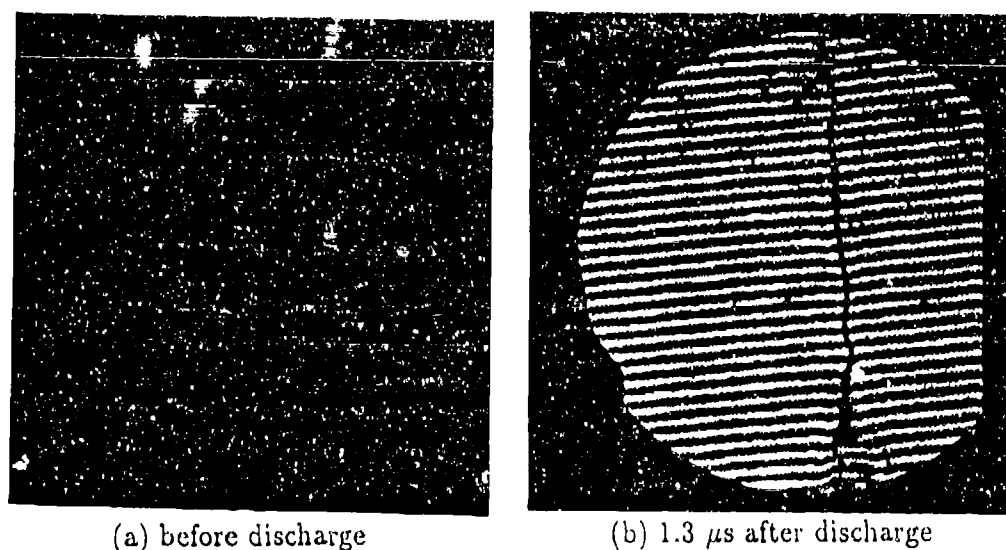
Figure 4-5. Interferograms taken before (a) and 1.3 μs after (b) a 15 kV discharge with a 33 μm carbon fiber.

Finally, in Figure 4-5, we show an example of what happens to the carbon fiber at low voltage. This figure shows two framed interferograms taken with a dye laser and a framing camera. One interferogram was taken before the discharge of the bank and the other (part (b)) 1.3 μs after the start of current. These were obtained using Electrode III for a charging

voltage of 15 kV. By comparing parts (a) and (b), one can see that the fiber has essentially not expanded 1.2 μs into the discharge when there was 60 kA flowing in the load. Some slight bending of fringes is observed near the cathode indicating plasma in that region. Other shots taken during the low voltage runs showed the fiber actually breaking at later times. This is strong evidence that the machine current never flowed through the body of the carbon fiber, but, through a path around the outside. Thus, a coronal plasma is observed without expansion of the fiber itself.

4.2 MEASUREMENTS OF SINGLE AL WIRE EXPLOSIONS.

A significant amount of data was taken on discharges with loads consisting of single 25 μm aluminum wires. The single wire explosions that were studied fall into four major categories; (1) those involving a direct discharge of the main bank, (2) those using the POS, (3) those using a preconditioner discharge only, and (4) those involving a combination of the preconditioner and a main bank discharge. The preconditioner was used to study the effects of altering the initial conditions and the POS to investigate the effects of changes in the current rise time. These measurements will be described in the following sections. Most of the main bank aluminum wire load shots that will be reported used Electrode IV and all of the shots involving either the preconditioner, or the POS, also used the Electrode IV configuration.

4.2.1 Measurements of Main Bank Discharges.

X-ray Measurements

As with carbon fiber loads, time resolved x-ray measurements were routinely made with GAD detectors. Figure 4-6 shows an example of one such a measurement taken on a 40 kV shot along with the load current. In this case the GAD was filtered with a 0.5 μm Parylene filter. As was the case with carbon fiber loads, these measurements were inconsistent with regard to signal magnitude and temporal location, but, the inductive dip in the load current close to peaks in the GAD signal was a consistent feature.

Observations with Imaging Diagnostics

Figure 4-7 shows two of our standard time integrating imaging diagnostics with a single 25 μm aluminum wire loads, in both these photos the load length was 2 cm. Part (a) is a photo from a x-ray pinhole camera, with a 30 μm pinhole, filtered with a 0.5 μm Parylene
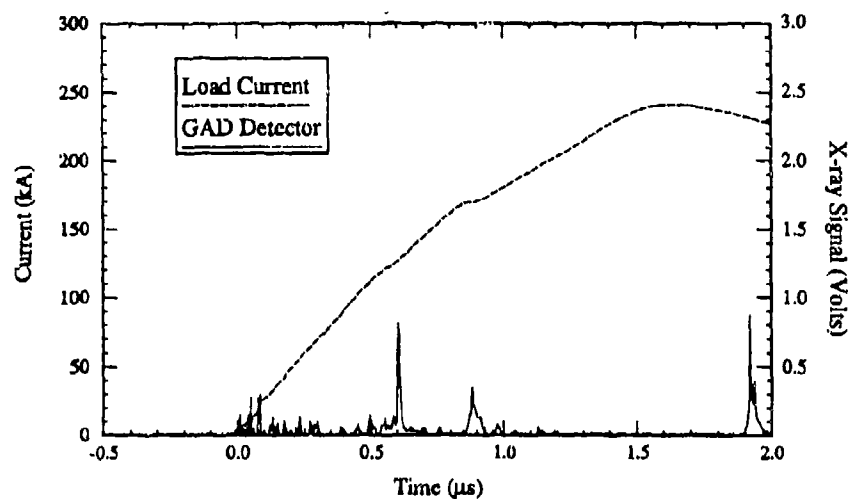
Figure 4-6. A signal obtained on a GAD detector with a 25 μm aluminum wire, the load current is also displayed. The shot used Electrode IV, the charging voltage was 40 kV, and the diode filter was a 0.5 μm Parylene foil coated with 800 Åof aluminum.
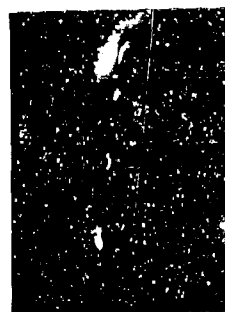
(a) x-ray camera
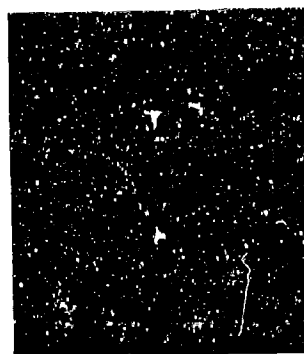
(b) optical camera

Figure 4-7. Photos of a 25 μm aluminum wire explosions with open shutter cameras for, (a), a 0.5 μm Parylene filtered x-ray pinhole camera at 35 kV and, (b), a neutral density filtered optical camera at 25 kV.

filter. The charging voltage was 35 kV. This shot is quite different from the x-ray pinhole camera shots taken with carbon, it shows well defined regions of high emission, or "hot spots", typical of many of the Al wire load shots. This effect was much more pronounced than with the carbon fibers. The open shutter optical camera picture taken at 25 kV, shown in part (b), is also quite different compared to its carbon counterpart. The emission channel is observed to extend more radially than those taken with the carbon fibers.

Figure 4-8. An example of a streaked absorptiongram obtained with a 25 μm aluminum wire. The streak duration is 300 ns and it begins a few ns before the current pulse. Arrows marked i_c and i_f indicate an imploding compression wave and shock front respectively. Arrows marked e_c and e_f indicate the corresponding expanding quantities. Microdensitometer scans of the absorptiongram were made at times t_1, t_2, and t_3.

Figure 4-8 shows a streaked absorptiongram where the streak duration was 300 ns, the charging voltage 40 kV, and the load length 1 cm. This is once again very different from the results obtained with carbon. For these loads an absorbing region is observed to initially expand at about 0.5 cm/μs. After this initial expansion the, a leveling off or radial contraction of the absorbing region was typically observed. Many of these streaks were recorded, and common to many of them was a structure interior to the load, as observed in this example, during the expansion phase. This structure, which consists of radially alternating light and dark regions, was usually present for the first 100 ns of the streak. This radial modulation

in the absorption will be discussed in latter sections. Also common to many of these streaks were the observation of thin refractive shell either expanding or imploding radially.

A gated x-ray pinhole camera was also used to monitor the performance of the machine during operation. The emission during a 150 ns interval of the current pulse was studied by delaying the gating of adjacent striplines by 25 ns. Emission characteristics at different times in the 1.5 μs rise time of the current pulse were obtained by appropriately delaying the first stripline. The striplines also could be gated for simultaneous observation and differentially filtered. Figure 4-9 shows the result of a measurement where one stripline was filtered with a 5 μm Kimfoil and the other with a 8 μm Kapton foil. These were obtained from a 40 kV discharge where the load length was 1 cm and the camera was on from 400 to 600 ns after the start of current flow. One can see that the higher energy x-rays which make it through the Kapton filter, are emitted from very discrete axial locations while the lower energy emission is quite broad spatially. It should also be pointed out that detection through the Kapton filter was never observed outside the 400 to 600 ns range as measured from the start of the load current.

Many double exposure holographic interferograms were taken of the wire explosions using either the Ruby laser or the YAG laser. Both of these essentially provided snap shots of the 2-D electron density at the time of the laser discharge. In addition, during reconstruction, a snap shot shadowgram could be extracted from the double exposure hologram which was essentially the same information that would have been obtained using a single exposure hologram. Figure 4-10 shows three interferograms taken at 116, 190, and 294 ns after the start of current respectively. These were all obtained from different 40 kV discharges with a 1 cm gap. Part (a) was taken using the Ruby laser and parts (b) and (c) with the YAG laser. Electron density information, which can be obtained by counting fringe shifts, will be discussed in a later section.

The general trends observed in these interferograms, which are representative of the large number that were taken, are an increasing channel width followed by an instability which was characterized by axial localization of the electron density. The channel remains relatively straight and uniform during the expansion phase, parts (a) & (b), up to about 200 to 250 ns into the discharge. After this time the interferograms show an axial nonuniformities which is characterized by localized electron density bunches and detachment from the cathode. The beginnings of this localization, as well as the detachment from the cathode, are illustrated in part (c). Interferograms taken later in time, i.e. later than 300 ns, were very complicated with many fringe shifts. They showed that the axial bunches expanded radially while other regions of the pinch did not.

This later time behavior was better illustrated using the snap shot shadowgram technique.
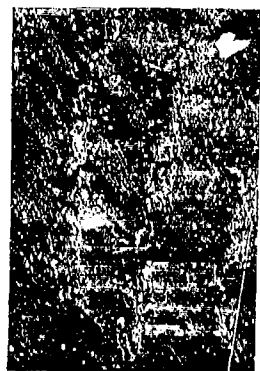
(a) Kimfoil   (b) Kapton

Figure 4-9. Results from a differentially filtered x-ray framing camera with an integration time from 400 to 600 ns after the start of current. Part (a) has a 5 μm Kimfoil filter and (b) has an 8 μm Kapton filter.
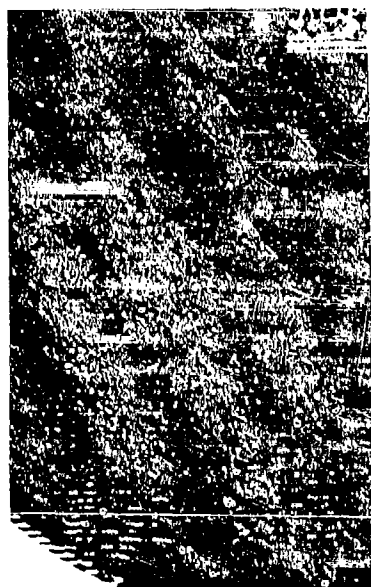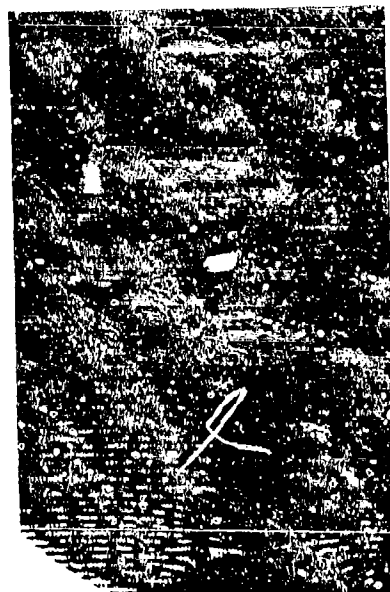
(a) 116 ns   (b) 190 ns   (c) 294

Figure 4-10. Reconstructions of double exposure holograms using a short pulsed laser on 40 kV shots with 25 μm aluminum wires. Parts (a), (b), and (c) were taken 116, 190, and 294 ns after the start of current, respectively.

43
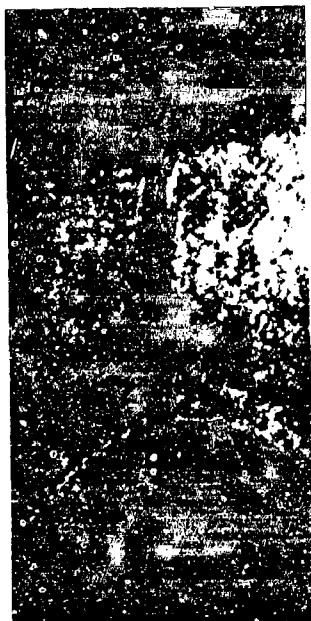
(a) 78 ns   (b) 254 ns   (c) 360 ns

Figure 4-11. Framed shadowgrams obtained during reconstruction of holograms made with the short pulsed YAG laser on 40 kV shots with 25 μm aluminum wires. Parts (a), (b), and (c) were taken 78, 254, and 360 ns after the start of current, respectively.
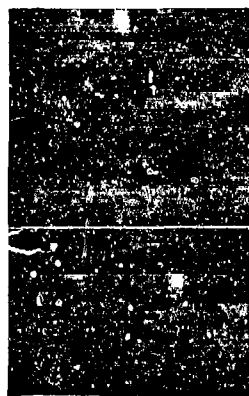
Figure 4-12. Photo of a 25 μm aluminum wire explosion with an open shutter x-ray pinhole camera at 45 kV with a 0.5 μm Parylene filter.

Figure 4-11 shows three shadowgrams taken with the YAG laser at 78, 254, and 360 ns into the discharge. Once again these photos were obtained from explosions where the main bank was charged to 40 kV and the load length was 1 cm. The same trends observed in Figure 4-10 are observed here. The onset of axial localization is shown in part (b) at 254 ns and the growth of the instability resulting in a series of radially constricted and expanded regions illustrated in part (c) at 360 ns.

4.2.2 Measurements of Discharges with a POS.

The results in this section will be reported in a slightly different manner from the previous section. With the exception of the x-ray pinhole camera, all the measurements reported in this section were obtained on a single shot. This allows one to correlate the load current, GAD signal, streak absorptiongram, and x-ray framing camera sequence.

A typical result from the open shutter x-ray pinhole camera with the POS is shown in Figure 4-12. The camera had a 30 μm pinhole and was filtered with a 0.5 μm Parylene filter. The photo shown here is very similar to the photos obtained with the main bank only. The axial localized "hot spots" are still observed with perhaps a radially narrower emission region compared to the main bank only shots.

Figure 4-13 shows the load and generator currents for a 45 kV aluminum shot with the POS. In addition a signal obtained on the GAD detector, which viewed the load, is shown. The seven dotted vertical lines indicate the times when a x-ray frame was taken, and the streaked absorption information was gathered between the solid vertical lines. It can be observed that the load current rises to its maximum in about 130 ns producing an average of approximately 1 MA/μs of current through the load. This is nearly an order of magnitude greater then the value of 0.2 MA/μs typically observed with the main bank only. Some similarities in the GAD signals exist such as a dip in the load current near the detector peak. However, the multipeak nature of the x-ray detector, common to many of the main bank only shots, was typically not observed with the POS.

Figure 4-14 shows a 300 ns streaked absorptiongram whose timing with respect to the load current was indicated in Figure 4-13. That figure indicates that the load current begins approximately at the begining of the streak. The very bright regions, which start about half way through the streak, indicate the dominance of plasma emission over the dye laser backlight. One very interesting feature observed in this streak which was typical, was a slow radial expansion of the absorbing region followed by a very rapid expansion and implosion when the load emission becomes dominant. The rapid expansion occurs approximately where the load current dips.

45
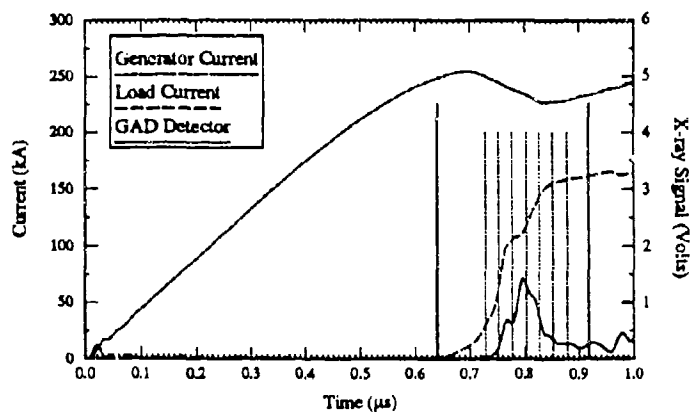
Figure 4-13. The generator current, load current, and signal obtained on a GAD detector for a POS shot at 45 kV and a 25 μm aluminum wire. The diode filter was a 0.5 μm Parylene foil coated with 800 Åof aluminum. The dotted vertical lines indicate the timings of the x-ray framing camera and the solid vertical lines indicate the duration of the streaked absorptiongram.

Figure 4-14. An ex   a streaked absorptiongram obtained with a 25 μ aluminum wire. The   duration is 300 ns and its duration is indicated in the figure above. Time advances from left to right.
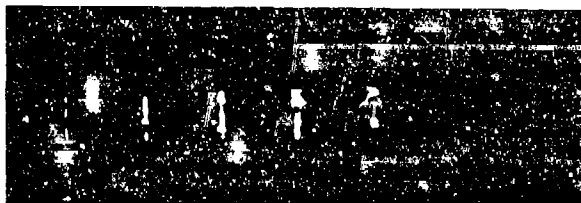
Figure 4-15. A sequence of seven x-ray frames, the integration time for each frame is 10 ns with the timings indicated by the dotted lines in the figure at the top of the page. A 0.5 μm Parylene filter was used.

46

The results from a sequence of x-ray frames is shown in Figure 4-15. Each frame integrates over a 10 ns period centered on the vertical dotted lines shown in Figure 4-13. This camera was filtered with a 0.5 μm Parylene foil. One can see that the emission increases becoming radially broader and more intense for the first four frames. The fourth frame, which corresponds to the peak in the GAD signal, apparently has the largest emission. These photos also roughly correlate with the streak results shown in Figure 4-14. The fifth, sixth, and seventh frames correspond to a period in time when the streak shows rapid expansion, and in these frames a reduction in intensity is observed.

4.2.3 Measurements of Preconditioning Discharges.

The preconditioning circuit attempted to heat the aluminum load to its vapor state prior to application of the z-pinch pulse. A number of diagnostics were fielded to determine the success of this effort. Visible emission spectra, interferograms, and streaked absorption and emission photography characterized its operation. Additionally, debris produced by the discharge was collected on quartz slides and analyzed using a SEM. Most work proceeded with the preconditioner charged to 20 kV, although some studies varied this voltage from 15 to 40 kV.

Visible Emission Spectra from the Preconditioned Loads

The visible spectrum collected with a spectrometer was recorded with a gated optical multichannel analyzer (OMA). For these shots, the OMA was gated "on" for 220 ns By starting the gate at successively later times during the discharge, snapshots of the emission spectra are pieced together to produce a time evolution of the emission. Six gated spectra in the 3900 to 4000 Å range taken during the preconditioner discharge are shown in Figure 4-16. Two neutral aluminum emission lines at 3944 and 3961.5 Å dominate these spectra, first becoming discernible over the background during the second time interval in the sequence. Other lines appear in some of the early time spectra, but not consistently through the discharge. The neutral aluminum lines were verified by demonstrating their absence when a carbon fiber was used in place of the aluminum.

Spectra were collected in other wavelength ranges in an attempt to detect Al$^+$ lines, but none were found. This does not imply that no ionization was present. The two neutral aluminum lines that were studied are strong ground state transitions. However, the Al$^+$ ion does not have any ground state transitions in the range of wavelengths detectable with this equipment, and those transitions that occur within this range may be too weak to detect.

The emission intensity of the 3961.5 Å line was measured as a continuous function of

47

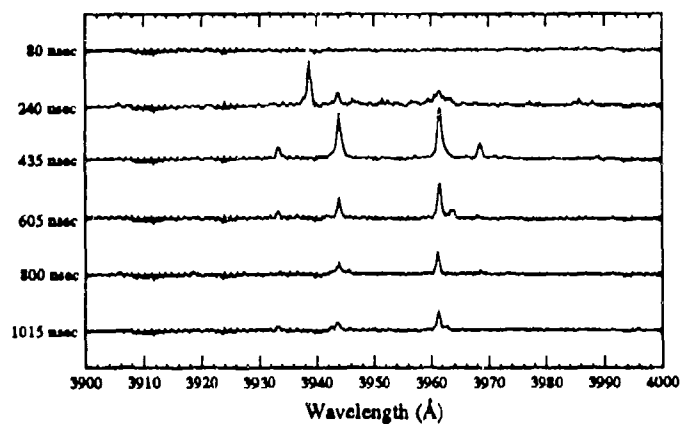Figure 4-16. Emission spectra from 540 mJ aluminum preconditioning pulses. Each spectrum is collected over a 220 ns gate period with the times at the left indicating the delay between the start of the preconditioner discharge and the start of the OMA gate.
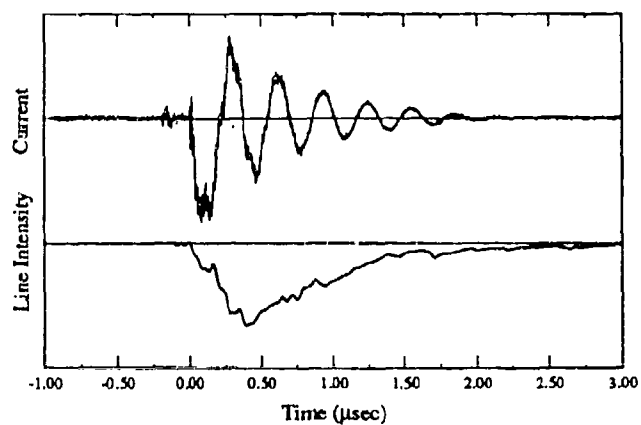
Figure 4-17. The intensity of the 3961.5 Å neutral aluminum emission line versus time as produced by a 540 mJ aluminum preconditioning pulse.

time using a monochromator with a PMT as the detector. A typical PMT signal and preconditioner current signal are shown in Figure 4-17. This result supports the results of Figure 4-16, showing an intensity that builds to a peak 500 ns after the discharge starts, and slowly diminishes.

Holographic Interferograms

Holographic interferograms of the preconditioner discharge were produced with a 50 ns ruby laser pulse. The same technique was used with a SF_6 gas jet in place of the preconditioner discharge to determine the direction of fringe bending for a neutral gas. A reconstructed holographic interferogram is shown in Figure 4-18. This hologram was produced 550 ns into the discharge which is coincident with the maximum neutral line emission. The fringes in the central region of the discharge bend in the same direction as was seen with the neutral gas jet. This indicated that the free electron density was quite low.
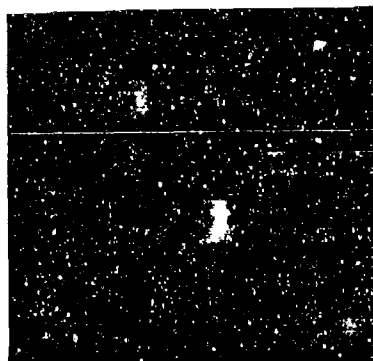
Figure 4-18. Reconstructed holographic interferogram of a preconditioned aluminum wire 550 ns into the pulse. One neutral fringe shift is seen in the center of the load.

Streaked Absorption and Emission Photography

A pulsed dye laser backlighted the preconditioner loads with 585 nm radiation. Neutral density and line filters were used to reduce emission from the discharge to a level far below that of the laser. The absorption of the load region was detected with a streak camera. A 1 μs duration streaked absorptiongram of a 20 kV preconditioner discharge is shown in Figure 4-19(a). A dark central region expands radially with a velocity 0.5 mm/μs.

A CW HeNe (633 nm) was used to backlight the load for longer streak durations. However, unlike the dye laser, the HeNe was not powerful enough to overcome emission from the discharge, and emission dominates during the first microsecond or two. A 30 μs streak

49

(a)   (b)   (c)
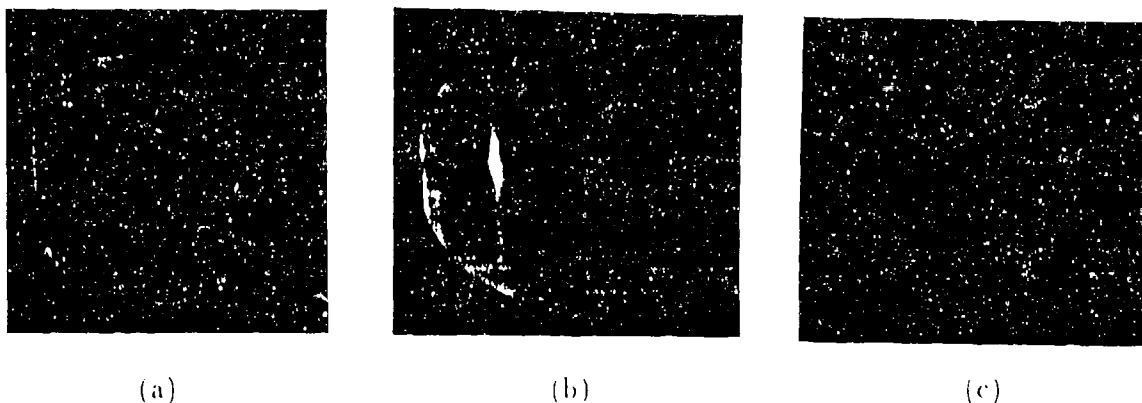
Figure 4-19. Streaked emission/absorptiongrams of preconditioned aluminum loads at a magnification of XX. a) 1 μsec dye laser streak of 20 kV preconditioner. b) 30 μs HeNe streak of 20 kV preconditioner. c) 100 μs HeNe streak of 15 kV preconditioner.

of a 20 kV preconditioner shot is shown in Figure 4-19(b). The broad region of emission is evident during the discharge (appromately two microseconds) followed by debris streaming out from the load. This feature is difficult to see at this charge voltage, but is very evident at a lower charge of 15 kV as shown in Figure 4-19(c).

(a) 15 kV   (b) 30 kV   (c) 40 kV
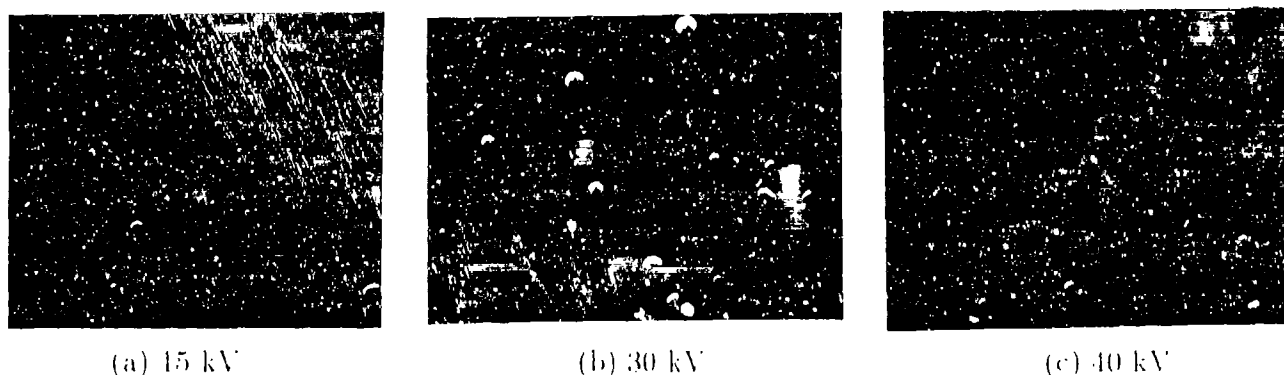
Figure 4-20. SEM images of debris collected from five preconditioner shots from 15-40 kV. The magnification is 200 for (a) and 5000 for (b) & (c).

Debris Collection

Quartz slides placed several cm from the load collected debris. Each slide collected debris from 5 or 10 successive shots. Using energy dispersive x-ray analysis (EDX) in conjunction

with the SEM imaging, the debris was characterized in both size and chemical composition. As the charge voltage was increased from 15 to 40 kV, the debris became finer, a result supported by HeNe streak pictures. Additionally, at higher voltages the aluminum seemed to be more molten at impact, producing a splattered pattern on the slide. SEM images of the debris collected from five preconditioner shots are shown in Figure 4-20.

4.2.4 Measurements of Discharges with Preconditioned Al Loads.

The aluminum wire preconditioner, described in the previous section, was used in conjunction with main bank discharges. Some differences were observed on the streaks and the double exposure holography, however, the other diagnostics showed essentially no difference from standard main bank discharges which have already been described. Therefore, in this section we will present the results of streaked measurements and double exposure holograms for preconditioned aluminum wire explosions. The data in this section used Electrode IV.
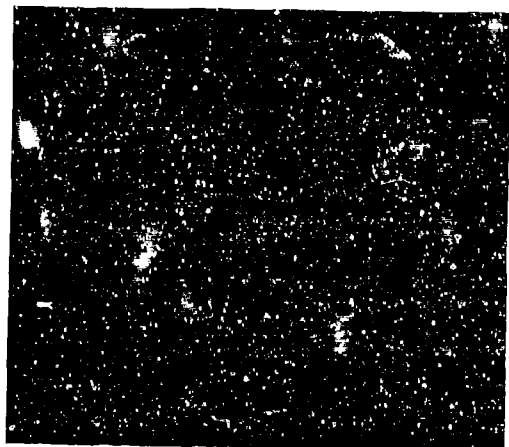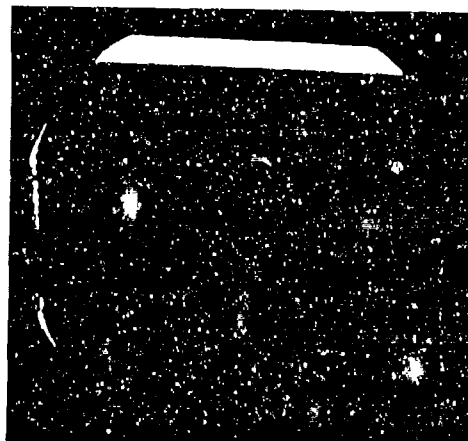
Streaked Absorptiongram Results

Figure 4-21 shows two streaked absorptiongrams taken on 40 kV discharges using aluminum loads that had been preconditioned. For these shots the preconditioner had been discharged 0.5 μs before the main bank current. Parts (a) & (b) were taken on two separate shots and have nominal streak durations of 1 μs and 300 ns respectively. Part (c) contains a representative load current signal in which the the start and end of the streak are delimited by solid and dashed vertical lines for the 1 μs and the 300 ns streaks respectively. In part (a), one can see the slow expansion of the bulk wire due to the preconditioner discharge which is followed by a very quick transition to an emission dominated medium. More difficult to see on this exposure is a thin shell, that expands much faster than the bulk absorbing region, which began near the start of the preconditioner current. A thin shell is also observed to implode onto the central region at the time the load becomes emission dominated later on in the streak. The main bank current began 175 ns before this occurred, and at shell implosion there was ~35 kA flowing in the load. The shell is observed very clearly in part(b), which is a more detailed streak around the time the shell has reached the axis. The timings of the shell implosions for the two shots fall within 5 ns of each other as measured with respect to the start of the main current pulse. This event (i.e. the implosion) is indicated by the "X" in Figure 4 21(c). The velocity of the shell, as measured from part (b), was 1.2 cm/μs. Extrapolating linearly and assuming that the radial implosion began at the start of the main current, the initial shell radius would have been 2 mm.

(a) 1 μs streak

(b) 300 ns streak
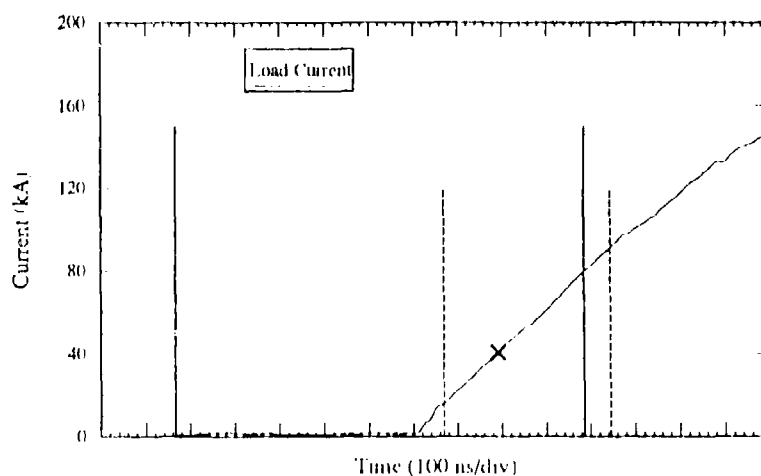
(c) load current trace

Figure 4 21. Two streaked absorptiongrams are shown in parts (a) & (b) and a represen
tative load current trace in part (c). The solid vertical lines delimit the streak
timing from the photo in (a) and the dashed lines for the photo in (b). The
"X" marks the time of the thin shell implosion observed in both photos.

Figure 4-22. Reconstruction of a double exposure hologram made from a 25 μm aluminum wire explosion that had been preconditioned. The picture was taken 137 ns into the discharge and the charging voltage was 40 kV.

Holographic Interferograms

Another interesting difference with and without the preconditioning was observed on the double exposure holograms. In particular, holograms taken relatively early into the main current discharge also showed the presence of a thin shell. An example of this is shown in Figure 4-22 which was taken 137 ns after the start of the main bank current. Although the shell is not uniform axially, it is clearly observed. The radius of the shell in this picture is approximately 1 mm but varies between 1.3 and 0.7 mm depending on the axial location.

4.3   MEASUREMENTS OF DOUBLE AL WIRE EXPLOSIONS.

In addition to carbon fiber and 25 μm aluminum wire loads, experiments were undertaken using two 25 μm aluminum wires as a load. Since two wires carrying parallel currents mutually attract each other, these experiments investigated the effects of this force on the mass of the wires. The single and double exposure holographic photography was best suited

for the investigation of this interaction. The loads were oriented so the two dimensional image created by these diagnostics was in the initial plane of the wires. Each wire was nominally 1 cm long and they had a separation that was 2.5 mm. With this orientation, wire mass that may accumulate between the wires, or radial motion of the bulk mass could be observed. The double wire loads were exploded with main bank discharges with and without the use of the POS. As with all other load types, x-ray measurements using the GAD detectors were routinely made, however, these signals were virtually identical to those with single wire loads. Reporting these measurements in this section is therefore unnecessary. The preconditioner was not used for these experiments which were carried out on the Electrode IV system.

4.3.1 Double Wire Explosions with the Main Bank.

Our observations using the double wire loads with main bank discharges are summarized in Figures 4-23 & 4-24 which each show two interferograms and framed shadowgrams respectively. These were obtained on 40 kV discharges. Figure 4-23(a) is an interferogram taken 220 ns into the start of the current. It shows that each wire has expanded substantially from its initial radius but that there is almost no mass between the wires or change in the wire positions. The latter observation is based on a hologram taken before the shot (not shown), which precisely determined the initial position of the wire. Furthermore, based on the direction of the fringe shifts in the centers of each wire, the bulk of the wire appears to be dominated by neutral matter. The shadowgram shown in Figure 4-24(a) essentially confirms the first observation that no mass has accumulated on axis at this time. This was taken on a separate shot 225 ns into the current pulse. Considering each wire independently, the interferogram at 220 ns is very similar to single wire interferograms taken between 100 and 150 ns into the pulse. This is not surprising since the current per wire in the two cases was about the same.

Later into the current pulse, Figures 4-23(b) & 4-24(b) show further expansion of the wires with some accumulation of mass on axis. Both of these photos were obtained from the same shot at 335 ns after the start of the current. The interferogram clearly shows fringe bending due to electrons between the wires and the shadow effects of this density is observed in Figure 4-24(b). Even though the effect of the mutually attractive force is observed, the bulk masses of the wires have not moved from their original positions. This was once again determined by measuring the exact initial wire positions prior to the shot. This lack of bulk motion and accumulation of mass between the wires is observed in both photos, but, is more transparent in the shadowgram.

Figure 4 23. Two holographic interferograms taken with double Al wire explosions using the main bank. Parts (a) & (b) were taken 220 and 335 n after the start of the current respectively.

Figure 4 24. Two framed shadowgrams (single exposure holograms) taken with double Al wire explosions using the main bank. Parts (a) & (b) were taken 225 and 335 ns after the start of the current respectively.
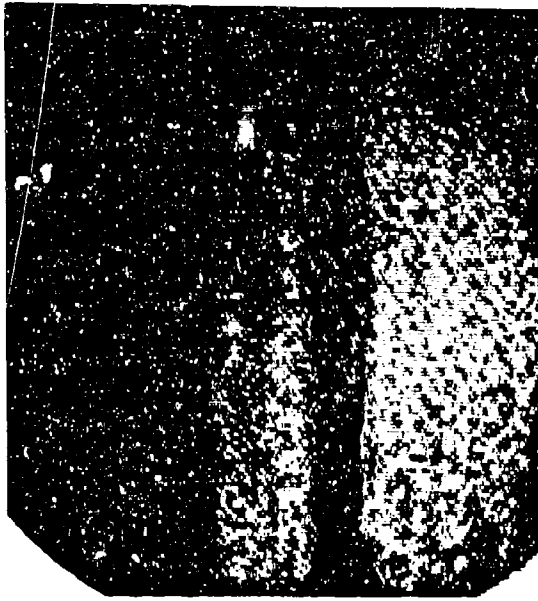
Figure 4.25. Two holographic interferograms taken with double Al wire explosions using the POS. Parts (a) & (b) were taken 58 and 160 n after the start of the current respectively.
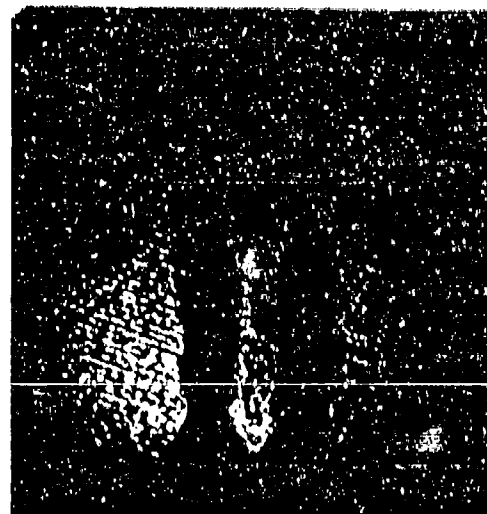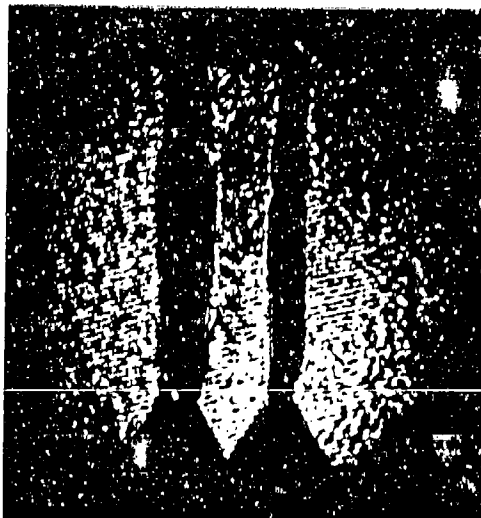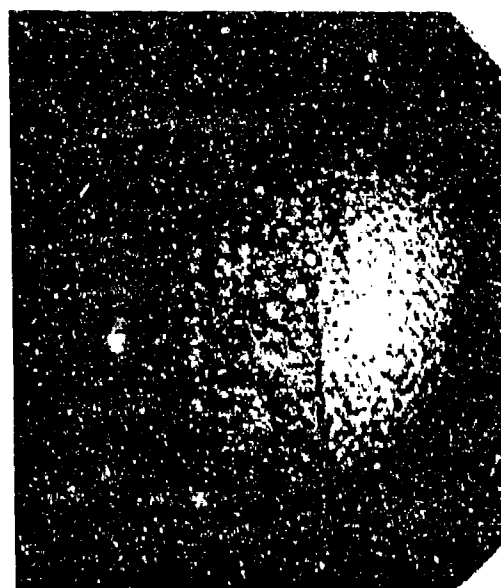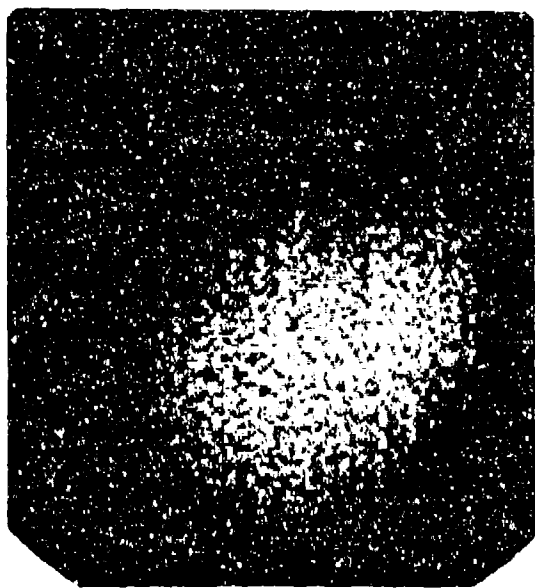

Figure 4.26. Two framed shadowgrams (single exposure holograms) taken with double Al wire explosions using the POS. Parts (a) & (b) were taken 160 and 235 ns after the start of the current respectively.

4.3.2   Double Wire Explosions with the POS.

The observations using the double wire loads with our POS are summarized in Figures 4-25 & 4-26 which each show two interferograms and framed shadowgrams respectively. The double exposure interferogram shown in Figure 4-25(a) was taken 58 ns into the opening. At this time there would have been approximately 30-40 kA of current in each wire. One can see that essentially nothing has happened to the wires, no expansion, fringe bending or movement is observed. The interferogram in part(b) of the figure, which was taken 160 ns into the opening, shows accumulated mass on axis as well as individual expansion of each wire. However, the mass accumulation in the center is very nonuniform axially. This is further illustrated in Figure 4-26(a) which is a shadowgram obtained from the same shot as part(b) of the preceding figure. The shadowgram shown in Figure 4-26(b) was taken much later in time, at 235 ns after the opening of the switch. One can see that the wires have expanded more and more mass has accumulated on axis. The axial nonuniformity of this mass is still observed but bulk shadows of the wire in its original position are also still observed. There are some significant differences between the POS and non-POS double wire explosions. With the opening switch more mass accumulates on axis faster with the expansion of the individual wires much less. However, in both cases, shadows of the wires in their original radial position are observed late in the respective current pulses indicated that the bulk mass has not been accelerated.

4.4   MEASUREMENTS OF WIRE ARRAYS.

The results obtained with the carbon and aluminum loads indicated that the current flowed in a hot, low density, corona outside a cold and maybe only partially ionized core. These observations were consistent with two wire measurements showing the corona imploding ahead of the core. The Mg on Al wire load experiments were designed to determine how important these effects would be on a terawatt class simulator using imploding wire arrays. The object of these studies was to determine how much straggling there was in the assembly of the load mass on axis. Our strategy was to evaporate different thicknesses of Mg on an Al core, keeping the load mass constant at a value consistent with optimum yields observed on pure Al wire arrays. The K-spectra of these elements are close enough to be simultaneously recorded on a time resolved crystal spectrograph, or on a McPig for VUV spectrograph. The spectrographs were aligned to view the central few mm radius along the array axis to determine when the different elements arrive. The McPigs were also aimed to view the original wire location to determine how long a current channel persisted there.

Loads with the following percentage of Mg and Al were tested: 10/90, 20/80, 30/70,
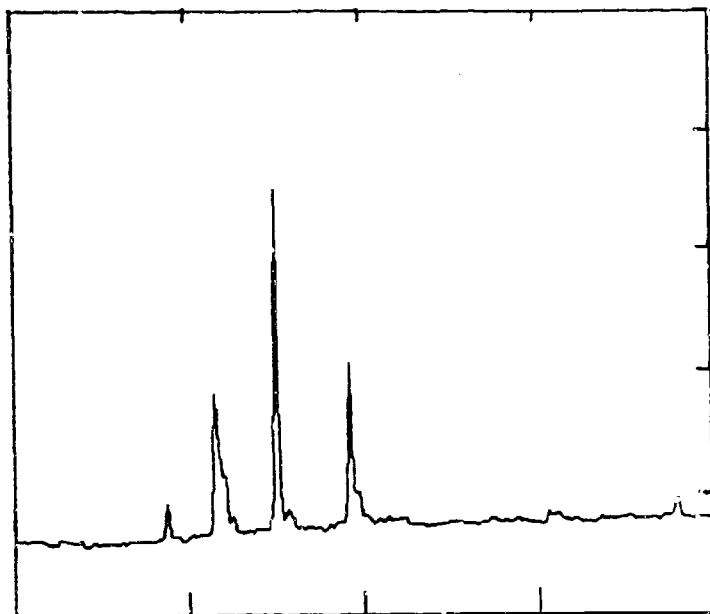
Figure 4-27. K-spectrum of the radiation emitted by an array with 70% Mg/30% Al wires. The lines from left to right are: 1S-2P Al XIII at 7.173 Å, 1S^2-1S2P Al XII at 7.806 Å, 1S-2P Mg XII at 8.421 Å, and 1S^2-1S2P Mg XI at 9.168 Å.
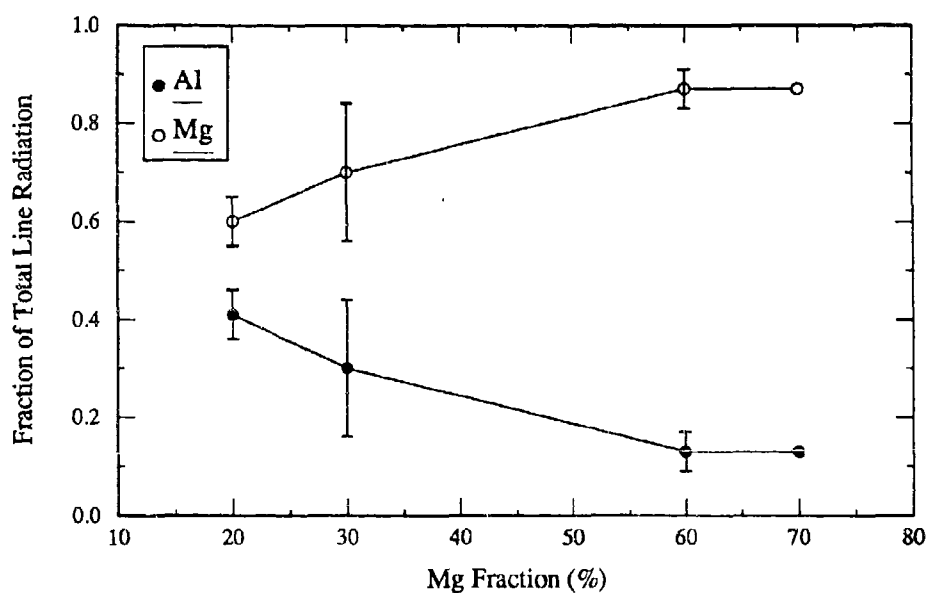
Figure 4-28. A plot of the fraction of the total K-spectrum line radiation in Al (solid dots) and Mg (open circles).

50/50, and 60/40. The x-ray yields from these loads were compared with the yield from 100% Al wire loads. The loads were imploded on the Double Eagle simulator delivering a peak current of 4 MA in a current pulse with a rise time of 100-120 ns. Besides the spectrographs, the implosion dynamics and x-ray yields were monitored with gated microchannel plate multiple pinhole cameras, open shutter pinhole camera, and GaAs photodetectors filtered to study radiation yields in the K-spectrum energy range of Mg and Al.
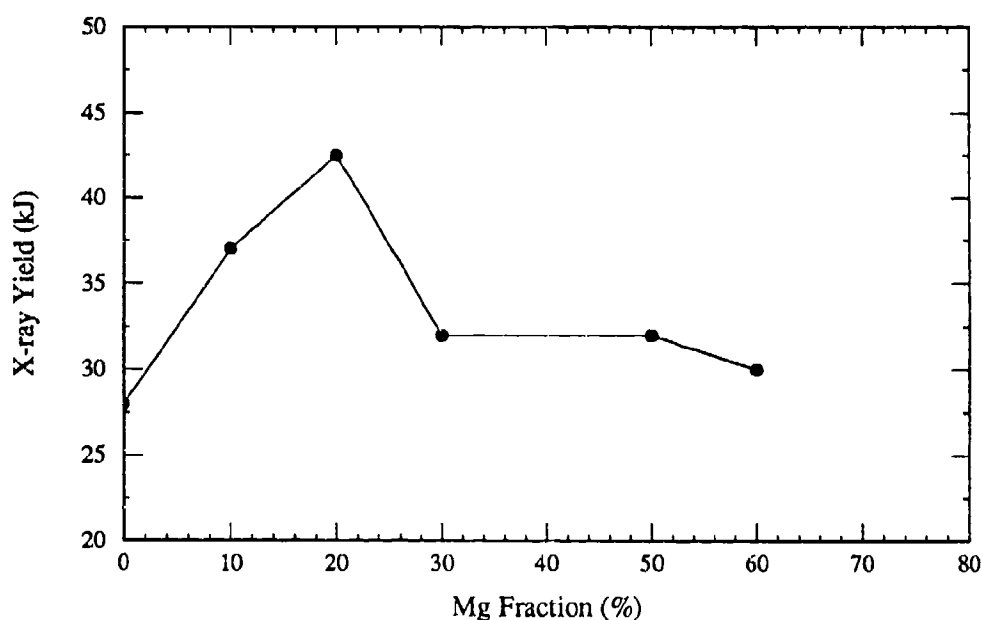
Figure 4-29. Plot of the x-ray yield versus the Mg fraction in the load. This data was obtained for wire array loads on the Double Eagle machine at Physics International.

A typical x-ray spectrum is shown in Figure 4-27. This spectrum, together with the filtered diode signals, were used to determine the relative amount of radiation emitted by the Mg and Al constituents. A rough estimate of the energy in each spectral component was obtained from the peak amplitude of the line using the measured response of Kodak direct exposure film published by Henke *et al.*.[39] The fraction of total line radiation that was due to the aluminum K-spectrum and magnesium K-spectrum, was determined for each load configuration. The average values are presented in Figure 4-28. This analysis includes the response of the 8.3 μm Kapton filter used, but, did not include variations in the diffraction

59

efficiency of the crystal with wavelength. The x-ray yield from the load was estimated from the filtered calorimeter signal. A peak yield is clearly observed in Figure 4-29, which displays these results.

Additional information about the plasma conditions in the pinch can be inferred from the measured spectra. If the plasma is optically thin, so that self absorption effects can be ignored, traditionally line ratio techniques can be employed.[40] If the electron density is known from other measurements, the ratio of the hydrogen-like to helium-like line intensities can be used to infer the plasma temperature. Since this line ratio has been measured for the Al and the Mg spectra in this experiment, the electron densities and temperatures can be infrared separately. Plasma temperatures in the range of 143 to 600 eV and electron densities in the range of $1 - 3 \times 10^{19} \text{cm}^{-3}$ have been determined using this procedure. The ratio of the Al to Mg helium-like intensities have been used along with the inferred electron temperature, to determine the ratio of Al to Mg helium-like ions in the ground state of the pinched plasma. The results are presented in Figure 4-30 for the range of load compositions studied here.
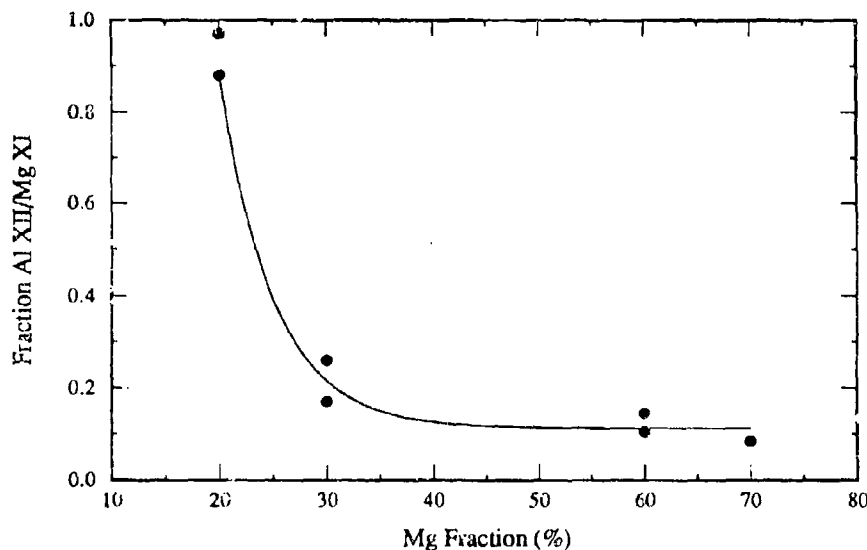
Figure 4-30. A plot of the x-ray emission of helium-like Al to helium-like Mg ion versus the percentage of Mg in the load wires. This data was inferred from a line ratio analysis of the measured K-spectrum.

SECTION 5

DISCUSSION

5.1 ALUMINUM.

The high resolution diagnostics used in these experiments reveal numerous interesting features of the Z-pinch dynamics. Some of these features, such as periodic expansion and contractions of the plasma column, have been observed before and have been attributed to n=0 sausage instability while others are new.[35] The most interesting new feature is the significant amount of radial structure that occurs in the discharge channel, as seen in the streaked absorptiongrams.(Figure 4-8) The highly absorbent core is surrounded by thin refractive shells (multiple shells in many cases) which implode on to the core while the core is expanding. In some cases, these shells appear to propagate through the core as a shock wave without significantly affecting the core, as seen in Figure 4-8. In other cases, the impact of these refractive shells results in sudden expansion or contraction of the core that can be accompanied by emission of radiation. Furthermore, the holograms indicate that the central core is often neutral atoms and the gated pinhole cameras reveal the emission of UV and soft x-ray emission (<300 eV) to come from hollow shells, while the keV radiation comes from localized "hot spots".

The exact relationship of the core, refractive shells, emission volumes, pinch locations, etc. is difficult to determine unambiguously since all of the diagnostics were not always fielded, and it was a fortuitous coincidence when a hologram and gated pinhole camera picture were recorded at the instant when a large x-ray emission pulse was observed. The relationship of these various features can only be inferred on a statistical basis in general.

The expansion and implosion velocities of various plasma features described above have been determined from a large number of streaked absorption and emission measurements. These are presented in Table 5-1. The magnitudes of these velocities fall into two ranges more than an order of magnitude different. The similarities of certain velocity components could indicate similar generator coupling and load dynamics effects while contrasting characteristics could imply the converse. These will be discussed according to the pulse power mode and number of wires in the load.

61

Table 5-1. Expansion velocities (cm/μs) of the core and refractive shell observed by streaked absorption on emission techniques at times a). t=0 when main bank fires or POS opens or b). t=t_1 when significant feature observed (wire appears to blow up or refractive shell implodes on axis).

	t = 0		t = t_1		
	Core	Ref. Shell	$t_1(\mu s)$	core	Ref. Shell
Bank Only Absorption	0.3 - 0.7				
Preconditioner Only Emission	0.21 - 0.23				
Absorption	0.012 - 0.062	0.27			
Precon. + Bank Absorption	0.03 - 0.07	0.28	0.17 - 0.25		-(1 - 1.5)
Bank + POS Absorption	0.02	Not Observed	0.11 - 0.33	1 - 1.4	

Main Bank with Preconditioner

At the initiation of the load current (t~0), the expansion velocity of the absorbing core is in the range of 0.01 to 0.07 when the preconditioner is fired alone or with the main bank. The expansion velocity of the emission front and the refractive shell, observed with the preconditioner, is significantly larger (0.2cm/μs for the former and 0.3cm/μs for the latter). These results suggest that refractive and emission fronts are one and the same and distinctly different from the absorbing core. Since the refractive shell responds to the main bank where as the core does not respond until the shell implodes on axis, this refractive shell appears to be a highly conductive plasma which shields the core from the main bank. This interpretation is substantiated by the holographic studies (Figure 4-22) where a thin plasma shell is observed around a primarily neutral core. The shell diameter (0.17 cm) is consistent with the maximum diameter that the refractive shell could achieve if it expanded at a rate of 0.32 cm/μs and imploded on axis 0.76 μs later with a velocity of 1.2 cm/μs. The actual trajectory produced by the magnetic forces is expected to be curved with a smaller maximum radius consistent with the observations.

If the expansion velocity of the core is taken to be an acoustic velocity, the observed value of 0.06 cm/μs implies a core temperature of 1074° K which is very close to the melting temperature of aluminum. These low values for the core temperature suggests that the core may not be fully vaporized. Since the sum of line densities in the thin plasma shell (1.8 to

6.3 x 10^{16}/cm) and in the neutral core (1 to 3 x 10^{16}/cm) represent less than 1/3 of the line density in the original wire, the remaining mass could be in the form of particulates. This is substantiated by the observation of the debris being emitted during a preconditioner shot and afterward, as seen in Figure 4-19c and 4-20, respectively.

Taken together, these results suggest the preconditioner pulse outgasses and vaporizes at least part of the Al wire. The surface expands and immediately breaks down when the density satisfies the Pashen voltage-pressure curve. This highly conducting plasma provides a short circuit path around the core leaving it cold and only partially vaporized. When the main bank is fired, the current initially couples to the plasma shell. The bank energy is transferred to the core when the shell implodes on axis as seen in Figure 4-21b. In some cases a relatively uniform expansion of the core occurs after the shell implodes, whereas, in other cases only the outer surface expands significantly following implosion.

Gated pinhole photographs taken about 150 ns after the shell typically implodes on axis reveal a soft x-ray (E ≤ 300 eV) emission regions having considerable radial and axial structure with a diameter varying from 0.6 to 0.9 cm. Simultaneously recorded photographs filtered with Kapton reveal the harder x-rays (E > 1 keV) to be emitted from narrow ribbons about 0.06 cm in diameter and 0.3 cm long. This diameter is very cl e to the diameter of the core when the shell implodes and could represent emission by hot coronal electrons impinging on the dense core.

This configuration of a plasma shell imploding on a cold core is very similar to the puff on wire experiments recently reported by Wessel et al.[5] They inferred better plasma stability and improved coupling to the generator. The enhanced stability could be due, in part, to a persistent cold core, similar to that observed here. They also observe enhanced x-ray emission, which again could be due to energetic electrons from the imploding shell impinging on the dense wire.

Main Bank with POS

The interpretation made above for the preconditioner studies has some important implication for interpreting the POS studies because of the similarity in the expansion velocities of the core under these two conditions (See Table 5-1). Even though interferograms were not taken of the POS plasma to establish the existence of a conducting shell outside of the core, the absence of any significant response in the core to the current pulse for ~120ns (at which time an imploding refractive shell is often observed), implies its existence. This conducting shell could then carry a significant fraction of the current as well as shield the core. Although no origin for this shell has been identified it could be due to prepulse current

outgassing the load or to plasma accelerated from the POS to the load.

The soft (E < 300 eV) and hard (E > 1 keV) emitting regions provide additional information about the current conduction processes. In general the soft x-ray regions appear to be hollow shells with considerable filamentary radial structure. Emission volumes 0.24 to 0.4 cm diameter have been observed 60 ns into the load current pulse at which time a load current of 60 kA is flowing. simultaneously recorded hard x-rays radiate from a series of diffuse spots $\sim$ 0.02 cm in diameter that appear to be along the original wire. Since 60 ns is slightly ahead of the time when significant coupling to the wire occurs (typically at $\sim$ 110 ns), these x-rays appear to come from high energy electrons in the corona impinging on the core. Both the size of the soft x-ray region and expansion velocities that have been recorded (0.4-0.5 cm/μs) imply a hot plasma region well outside the wire volume. This coronal plasma may be the current carrying channel with many characteristics similar to those observed with the preconditioner.

Main Bank Experiments

The characteristics of the discharge channel produced by main capacitor bank are distinctly different from those observed with preconditioner or opening switch. Not only does the entire core appear to expand, its initial expansion velocity is larger than that observed with the other two pulse power modifications. These discharges were more completely diagnosed providing more detailed information about the discharge process.

The streaked absorptiongrams revealed a considerable amount of internal structure in the discharge channel not seen in previous studies. This is largely due to the fact that absorption is more sensitive to slight variations in density and temperature with the large magnification (x12.5) used to record the data playing an important role. In addition to the radial striations seen during the early expansion phase in Figure 4-8, considerable internal structure is observed right after the column pinches and begins to slowly expand. The arrow marked, i_c, point to a radially imploding boundary separating a dark absorbing interior core from a lighter, less absorbing outer layer. The boundary appears to expand radially after it crosses the axis and emerges at the point marked by the arrow e_c. The imploding boundary is followed by a thin absorption front that begins to implode at the arrow marked i_f. There is also an expanding absorption front marked e_f which could be a reflection of i_f front when it hits the axis.

To study this internal plasma structure microdensitometer scans were made of the film density at times marked t_1, t_2, and t_3 in Figure 4-8 which corresponds to times 113, 173, and 226 ns into the current pulse. The incident light intensity was inferred from film density

64

using the manufacturers published curves and Abel inverted using a 40 point inversion routine developed by Bockasten.[28] A typical result presented in Figure 5-1, clearly reveals the radial structure seen in the streak photograph. The two earlier time scans(t_1 and t_2) have a smaller absorption coefficient on axis than in the wings. This is reversed in scan t_3 where the center predominates. A careful inspection of Figure 4-8 could indicate the reason for this change. Scan t_3 is taken at the time when the imploding boundary denoted by, i_c, has reached the channel axis, and the dark absorbing "core" is on axis.
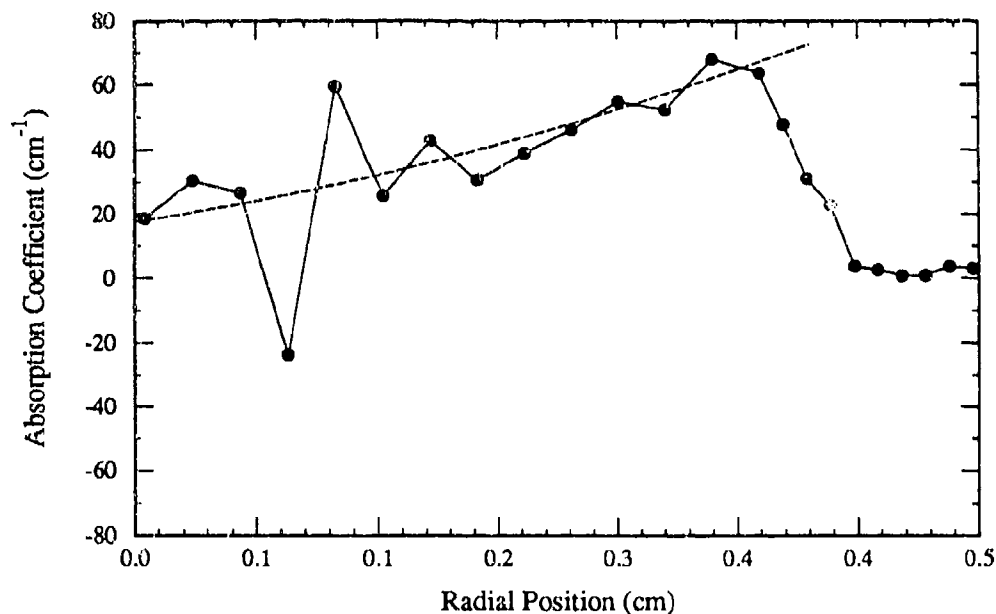
Figure 5-1. Radial profile of the absorption coefficient obtained by Abel inverting a microdensitometer scan of Figure 4-8 at t_2=173 ns.

It is important to establish whether the features seen in the photograph are representative of internal structure in the discharge column or are an artifact of the measurement technique. A ray from a collimated source traversing the plasma column can be absorbed or it can be refracted by gradients in the index of refracti n perpendicular to the trajectory of the ray. If this deflected ray misses the collection lens, a dark region appears in the image, giving rise to a "shadowgram".[32] Rays can also be focussed by negative index gradients giving rise to regions of enhanced intensity. It is difficult to determine if a given intensity profile is due to absorption or refraction processes.

65

The important question to answer is whether a single step function in index at the plasma edge or a thin annular index shell could produce the striated intensity profile observed throughout the interior in Figure 4-8 for $t \leq 100\ ns$. To determine this, a ray tracing model was developed to follow the trajectories of an initially collimated beam as they traverse an arbitrary index distribution. These refracted rays are then collected by an ideal lens and focussed. The intensity profile is then determined by coherently adding the contributions from individual rays. The results are presented in Figure 5-2 for a uniform plasma column ($n = 5 \times 10^{20}/cm^3$, r=0.3 mm) having a density scale length of $\delta \sim 5 \times 10^{-3}$ mm. A dark shadow is seen in the region of the column edge with a series of light-dark fringes in the interior. If the scale length of the density gradient is increased by a factor of 1.6 to 8×10^{-4} the fringes near the center disappear. Only one dark fringe is observed inside the broad shadow if $\delta = 1 \times 10^{-3}$. Similar effects are seen with an annular ring having a comparable scale length.
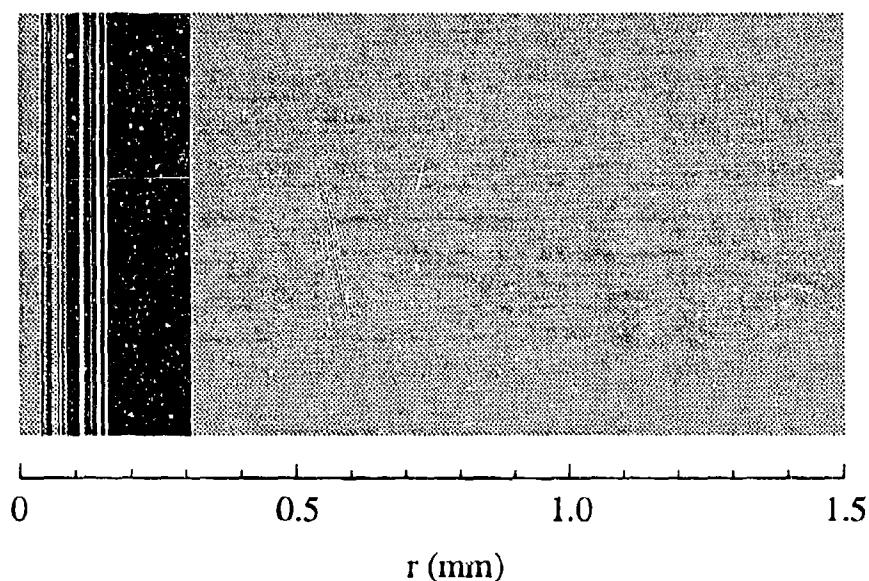
Figure 5-2. Predicted image of a uniform plasma column backlighted by a collimated laser beam. The density of the plasma column is 5×10^{20} cm^{-3}, its radius is 0.3 mm and the density scale length at the edge is 5×10^{-3} mm.

It is clear that the striations observed in Figure 4-8 could not be due to these refractive effects because of the unrealistic conditions that are required. The electron density in the simulation would require the average charge state to be 4.5 in the experiment. However the density scale length could not be preserved for the 50-100 ns over which the striations are

observed. The observed expansion velocity of 0.3-0.6 cm/μs would increase the scale lengths by more than an order of magnitude which would wash away most of these effects. Only the closely spare fringes seen at the bottom of Figure 4-8 might survive.

This simplified analysis strongly suggests that the internal features are real and not artifacts of the diagnostic technique. This is not to say that refractive effects are not important. Any region where a negative value is inferred for the absorption coefficient clearly has some focussing effects due to index gradients contributing to the intensity profile. A proper analysis of the data requires the observed intensity profile to be fitted by a calculated profile using a ray tracing model that includes both refractive and absorptive effects. The analysis carried out here will ignore the refractive effects.
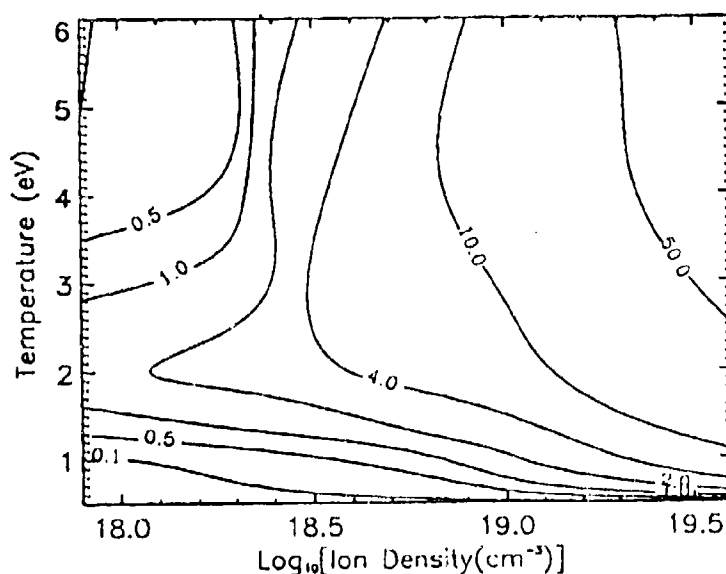
Figure 5-3. Calculated optical absorption coefficients (cm^{-1}) for aluminum at a laser wavelength of 585 nm (2.12 eV).[36]

Qualitative features of temperature and density profile can be inferred from measured absorption profile using the calculated absorption coefficients of J. Apruzese.[33] The absorption coefficients in Figure 5-3 are small at high density and low temperature ($T < 0.5\ eV$) or at low densities ($n \leq 2 \times 10^{18}$cm^{-3}) at almost all temperatures. It is reasonable to assume that the density decreases radially from a maximum on axis and that the temperature is low on axis and increases toward the edge of the column where ohmic heating is expected to heat the plasma to produce the large absorption wings seen in Figure 5-1.

To obtain more information about the density or temperature profiles requires an independent measure of either n(r) or T(r) or some model calculation relating the two. Unfortunately, the latter requires an expression for the plasma conductivity which is valid at low temperatures ($\leq$ 2 eV) and high densities $10^{19} - 10^{20}$ where the Spitzer relationship may not be valid.

In lieu of a model calculation, some information may be inferred about n,T profiles by assuming a profile for one variable and inferring the other. A Gaussian density profile, a constant temperature(isothermal) or a constant pressure(equilibrium), are some options. Some additional information is required to pin down a variable at one point. This may be achievable at the edge where the expansion velocity gives a handle on Z and T while the absorption relates T and n. Assuming the plasma edge expands at the ion acoustic velocity

$$C_s = \sqrt{\frac{\gamma KT(1+Z)}{M}} \tag{5.1}$$

the values of n=3.6 x $10^{19}/cm^3$, T=3 eV and $\bar{Z}$=1.5 gives the absorption coefficient of 60 cm^{-1} at the edge. Starting from this condition at the edge, and assuming the product nT is a constant, average value profiles for the density and temperature can be obtained by drawing a smooth curve(shown dotted in Figure 5-1) through midpoints of the oscillation. The results are presented in Figure 5-4. Also shown in that figure is a curve corresponding to density variation that would be required to produce the fluctuation in absorption observed if the latter is due to an adiabatic fluctuation in pressure ($Tn^{1-\gamma}$=constant). The total line density of atoms represented by Figure 5-4 is 2 x10^{17}/cm which is in good agreement with the line density of atoms in the Al wire (3 x 10^{17}/cm). The density and temperature on axis predict a value of $\bar{Z} \sim 0.23$ which is much less than the value of 1.5 at the edge.

Although a complete analysis of the radial density and temperature profiles is not available for our experimental conditions, the simplified analysis presented above is qualitatively consistent with our calculation and those of other authors. The calculations presented in Chapter 2 predict the plasma channel radius to be 0.05 to 0.06 cm at a time 40 ns into the current pulse which agrees well with our observations. This time corresponds to values of the load current which are comparable to those at which the absorption measurements were made. The temperature inferred from the absorption measurement ($\sim$3 eV) is comparable to the values in the corona calculated with the Cauble resistivity (5-10 eV) but not with that calculated with the Spitzer Harm resistivity (200-400 eV). In a similar fashion, Neudachin and Sasarov [16] have calculated the equilibrium profile in a high temperature diffusion regime where good thermal conductivity has resulted in an isothermal temperature distribution and a low conductivity regime where the coronal temperature is higher than at
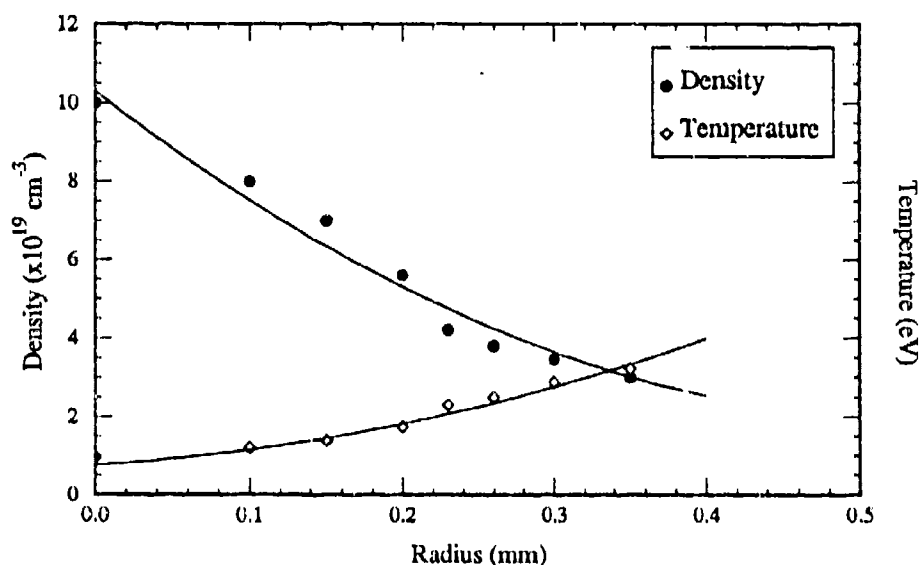
Figure 5-4. Radial density profile (solid circles) and temperature profile (diamonds) inferred from the average absorption profile assuming nT is constant. The dashed line from Figure 5.1 was used for the absorption profile. Here n is the density of ions plus neutrals.

the center. They obtain ratios of the corona to core temperatures that vary from 3 to 13 in the latter case. A coronal temperature of ~ 3 eV was predicted in both limits which agrees with the value we have estimated.

The interferometric measurements can provide information about the net distribution of electrons in the plasma relatively independent of their temperature. The term net is used to emphasize the fact that the change in index due to electrons is of opposite polarity to that of neutrals (or ions) and it the difference in these contributions which determines how the fringe is bent. Since the contribution due to neutrals is about 1/10 of that due to electrons, a 10% ionized plasma would have a zero net contribution to the index. With this caveat in mind, the evolution of the discharge channel proceeds as follows.

First a narrow channel ($d < 0.01$ cm dia.) is formed with a peak electron density of $4 \times 10^{19}/cm^3$. The channel is observed to expand with a neutral core appearing at 150 ns into the current pulse, at which time the current is 32 kA. The neutral core persists for 100 - 200 ns and is surrounded by a coronal plasma. The evolution of the electron and neutral densities is summarized in Figures 5-5 & 5-6 which also shows the line density of these two

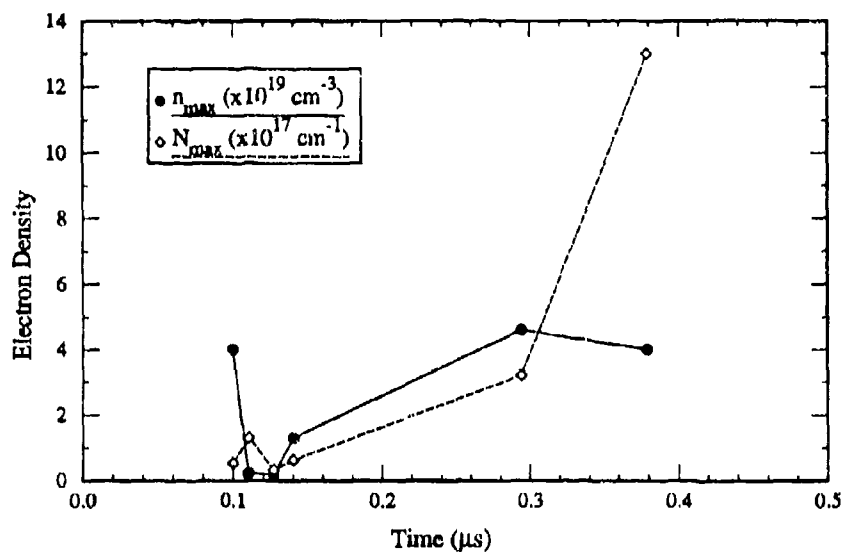Figure 5-5. Plotted are the number density (solid circles) and line density (diamonds) of electrons in the discharge channel as a function of time. Time zero is the start of the main bank current.
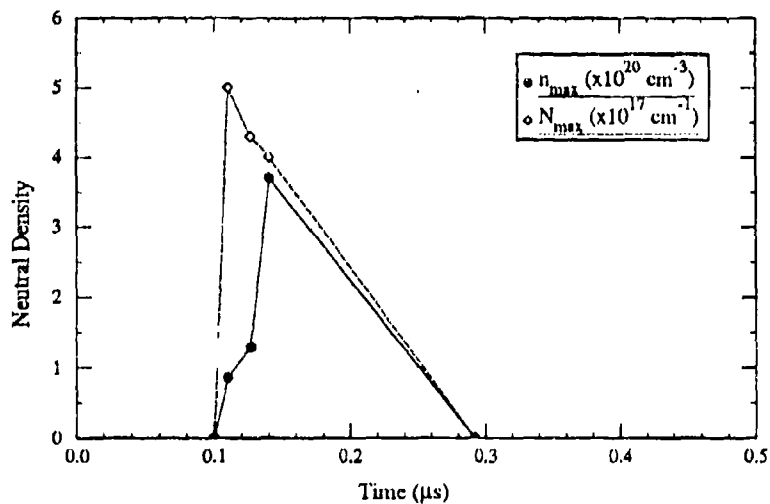

Figure 5-6. Plotted are the number density (solid circles) and line density (diamonds) of neutrals in the discharge channel as a function of time. Time zero is the start of the main bank current.

70

species.

Two comments are in order concerning these results. First of all, the line density of neutrals exceeds the 3.15×10^{17}/cm in the original wire. This is attributed to an incorrect estimate for the index coefficient of neutral Al vapor. The second comment concerns the appearance of a neutral core 150 ns into the pulse. This occurs after the channel has expanded and could be due to an adiabatic cooling associated with the expansion.
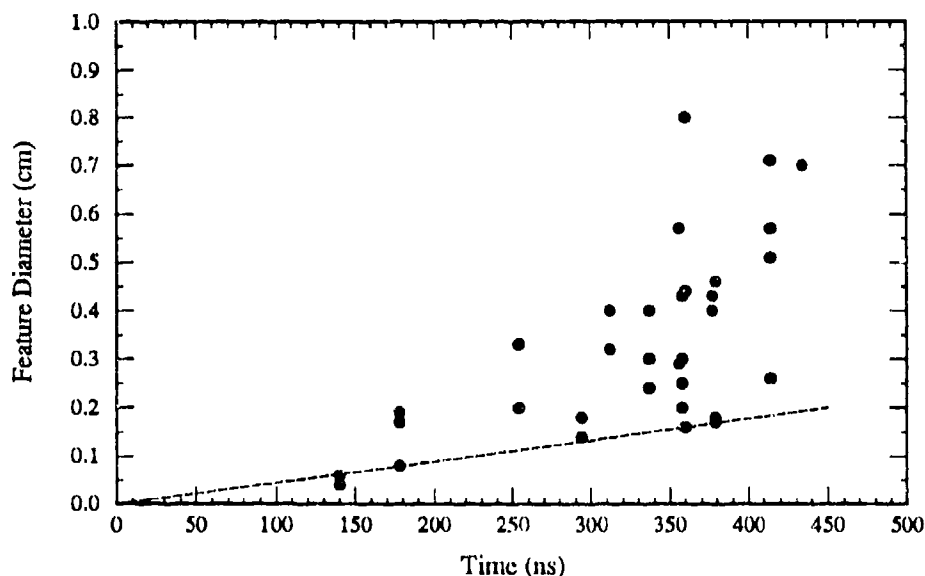
Figure 5-7. Diameter of plasma features observed on interferograms at different times in the discharge current. Dashed line represents range of expansion velocities inferred from absorptiongrams.

The well defined channel seen at early times becomes distorted with low density necked down pinch regions separating expanded bulges of dense plasma. The pinch stability characteristics was studied by measuring the radii of column bulges and constrictions observed at different times in these interferograms. Initially, the maximum and minimum radii were about the same and increasing at about 0.4 cm/μs comparable to expansion velocities observed with absorptiongrams. At about 200 ns, the maximum radii appeared to grow at a rate of 3 cm/μs. This is shown in Figure 5-7 and is associated with the growth of large scale inhomogenieties. The density in the neck regions, 2.4×10^{18}/cm^3, is more than an order of magnitude less than the 4×10^{19}/cm^3 observed in the bulges. These density minimum have

also been seen in other experiments,[34] where they have been linked to the m=0 sausage instability.

These plasma inhomogenieties appear to be associated with the emission of soft x-rays that are observed to occur in the 200 - 400 ns range at which time these inhomogenieties are rapidly developing. However, the role of these inhomogenieties in the x-ray emission process is not clear. Although m=0 sausage instabilities augmented by radiative collapse have been predicted to produce localized highly compressed plasma that can radiate as "hot spots" in high Z materials,[35] the density minima observed here suggest that a different mechanism must be functioning. The most obvious process is energetic electron beam production in the density minima producing nonthermal tail on the electron distribution.[36] To examine this idea attempts were made to correlate emission volumes observed with gated pinhole cameras and plasma features seen on interferograms. Unfortunately the exact location of the electrodes in the gated pinhole photographs was not adequately known, and a large number of simultaneous measurements were not available to obtain good correlation.

Two Wire Aluminum Loads

The interaction of two current carrying discharge channels was studied in the two wire load experiments. As the individual wires explode and begin carrying current they evolve in much the same way as the single wires. (See Figures 4-23 and 4-24) Again a neutral core surrounded by a coronal plasma is quite evident. The most dramatic and interesting feature of the two wire shots is a rapid flux of electrons into the intra-wire region. These electrons arrive early and have a significant density ($3 \times 10^{19}/cm^{-3}$) long before the two channels coalesce into a single pinch which thereafter looks similar to single wire pinches. This early run-in plasma is even more dramatic in shot when a plasma opening switch (POS) was used.(Figure 4-25) Here streamers appear to connect the wires in the intra-wire region. These are more apparent in shadowgrams made from the holographic interferograms.(Figure 4-26) In Figure 4-26 there is a serpentine density maximum in the intra-wire region which exhibits a peak fringe shift of 3 7. If one assumes that the depth of the plasma is on the order of the plasma channel diameters, 0.26 mm, then the average density is $5 \times 10^{19}/cm^{-3}$ and the line density is $2.7 \times 10^{13}/cm^{-1}$, or about 10 percent of the original load mass. These results demonstrate a significant fraction of the load runs in prior to any observable motion of the main plasma channels.

An interesting feature of these results is the plasma streamers bridging the gap between the wires. Similar streamers were observed by Kalentar and Hammer [37] between the wires in a X-pinch experiment. The precursor plasma quantitatively measured here has been

72

suspected to occur in plasma array implosions as early as 1981 by Pearlman *et al.* [38] and measured by Aivozov *et al.* [14] in 1985 using a laser probing technique. This is very important to simulator physics because they also observed x-ray emission on axis 15-40 ns before the array imploded.

The precursor plasma observed here is a natural consequence of a heterogeneous discharge channel where the hot coronal plasmas shields the interior of the channel from the magnetic field of the other wires in the array. This results in an acceleration that is largest on the low mass coronal plasma and smallest on the massive core inside. The light coronal plasma can now implode resulting in the observed precursor. This nonuniform acceleration processes on the coronal plasma has been discussed by Bobrova *et al.*.[12]

This precursor effect is expected to be more significant as the wire mass is increased. Both Lindenmuth *et al.* [11] and Bobrova *et al.* [12] have shown that the time, τ, required to vaporize and ionize a wire increases as $M^{1/2}$. Furthermore Bobrova also found that τ is proportional to $\dot{I}^{-7/12}$. This mass and $\dot{I}$ dependence will be much worse on very large current generators like Jupiter where significantly larger masses are required to meet the MR^2 scaling laws.

5.2 CARBON FIBER LOADS.

The discharge with carbon fiber loads were distinctly different from Al loads exploded by the main capacitor bank. The imaging diagnostics and interferometry, all showed a dense solid or neutral core that did not partake in the current conduction process. The line density of neutrals was observed to decrease from 3.4×10^{16}/cm to 4×10^{15}/cm as the current increased from 54 kA to 95 kA. These values represent 3.2 to 0.4 percent of the available atomic line density of 8.5×10^{17}/cm. For this range of currents the line density of electrons in the corona ranges from 8×10^{16}/cm to 1.1×10^{17}/cm implying that no more than 12% of the fiber was even vaporized.

At about 458 ns into the current pulse, several m=0 sausage type pinch regions are observed. Unlike the aluminum loads, these neck regions do not exhibit on axis density minima. The type of pinch stability has been attributed to the persistence of a solid core in deuterium fibers by Lindenmuth *et al.* [11] and by Neudachin and Sasarov.[16] These later authors attribute this stabilization process to a localized evaporation of the core at locations where the pinch neck comes in contact with the surface. This phenomena is clearly evident in Figure 4-1 ' where a thin refractive shell, imploding on axis, is observed to bounce off the surface with a burst of visible radiation emitted when contact is established.

5.3 MAGNESIUM COATED AL LOADS ON DOUBLE EAGLE.

The magnesium coated Al load studies were carried out to see how many of the effects observed in these low energy, low power experiments, carry over to the high power simulators and what impact they have on simulator efficiency and performance. Although the collisional radiative equilibrium modeling, to relate the observed spectrum to the plasma condition in the pinch, is outside the scope of this work, a few observations based on a simplified equilibrium analysis can be made. First of all, enhancement in the yield at 20/80 percent composition of Mg and Al was unexpected and is not understood. On the other hand, the decrease in Al K-shell lines that is observed when the percentage, and hence thickness, of the Mg coating increases was both anticipated and is consistent with the heterogeneous load characteristics observed in the in-house studies. The relative absence of Al K lines when the Mg composition exceeds 40-50 % indicates the absence of significant quantities of He-like and H-like Al ions on axis during radiation pulse. This in turn implies that only the outer 10 μm of Mg coating imploded leaving an Al core $\sim$20 μm in diameter to implode at a later time. This is clearly consistent with the observed implosion of the outer corona in the two wire load studies described above, which left most of the core at its original location. It is also consistent with the conjecture, by Deeney et al., that all the load mass does not appear to radiate in the K-shell.[8]

The line ratio analysis presented in Section 4.4 is valid only if local equilibrium conditions prevail and the plasma is optically thin. The latter is easily satisfied for the electron densities (few $\times 10^{19}$cm^{-3}) and plasma temperatures (140-500 eV) inferred from the line spectra. The optical absorption length for the line radiation due to resonance effects alone is about 0.3 cm, which is larger than the radius of the pinched plasma column. Since this should be the dominant absorption process, the assumption of an optically thin plasma is not unreasonable. On the other hand, the inferred electron densities are not commensurate with an eleven times ionized plasma in local thermodynamic equilibrium at these temperatures. In spite of this inappropriate application of the LTE model, the plasma parameters inferred may not be all that far off their mark. The inferred electron density and observed pinch radius of 0.1-0.15 cm, implies an ion line density in the range of 9×10^{16} to 2×10^{17}cm^{-1}. This is consistent with all the mass in the Mg layer and an equal Al mass for a 20/80% Mg-Al load. The fraction of helium-like Al and Mg predicted by this analysis are equal at the 20% Mg load configuration as seen in Figure 4-30. This self consistency in the parameters encourages confidence in the reasonableness of the analysis.

The ramification of these results on our understanding of array physics and simulator

74

efficiency is significant. The good agreement between the observed and calculated implosion time has been taken as evidence that the entire mass imploded as calculated and that the kinetic energy anticipated had been developed. The calculated kinetic energy could only account for $\sim 1/3$ of the radiated energy.[10] If the actual mass imploded in the same time interval is less than the total mass, then the on axis kinetic energy is less and this energy deficit is even larger.

The effect that this has on the simulator efficiency can be understood by an examination of the relationship between the implosion time Δt, the load mass M, array radius R, and machine current I. This equation is

$$\Delta t = A\sqrt{M}\frac{R}{I}, \tag{5.2}$$

where A is a constant. If one half the mass is observed to implode in a time Δt_1, which is equal to the time Δt_o that is predicted for the entire mass M_o by (5.2), then the actual driving current I_1, is less than the total current I_o, i.e. $I_1 \sim I_o/\sqrt{2}$. Since the magnetic energy stored in the gap is proportional to LI^2, only half of the machine energy goes into imploding the radiating portion of the load. The remainder flows through the residual core of the wires and may implode at a later time. It is clear that any such division in the currents will result in generator losses and reduced radiation yield.

SECTION 6
CONCLUSIONS

The salient features of this study can be summarized as follows:

1. HY-Tech has demonstrated the usefulness of high resolution imaging diagnostics to study plasma phenomena at densities approaching $10^{20}/cm^3$. Small numerical aperture lenses have been used to magnify the image and to overcome refractive effects plaguing other studies. A detailed view of the discharge channel produced by an individual wire has been obtained using laser back lighted absorption and interferometric techniques. A framed mode has been used to obtain a 2-dimensional view of the entire pinch and a streaked mode has been used to study the radial pinch dynamics at one axial location.

2. A heterogeneous discharge channel was observed with a low density coronal plasma surrounding a dense core which may be solid or only partially ionized for a significant fraction of the discharge current. The core in the carbon fiber load studies showed the smallest participation in the conduction process. The coronal plasma seem to be a surface discharge and associated with out gassing phenomena in the carbon case. Under similar conditions aluminum wires exhibited a rapid expansion and subsequent contraction demonstrating magnetic pressure effects on the main core. The response of an aluminum wire to the generator pulse appear to be more like the carbon case if an opening switch was used to increase $\dot{I}$ or a small preconditioner pulse was used in an attempt to prevaporize and preionize the wire. No interaction with the core was evident until a coronal plasma was observed to implode on axis.

3. In two wire experiments, a precursor plasma was observed to separate from the wires and implode on axis while the bulk of the wires remained at their original location. This effect was exacerbated when a POS was used to increase $\dot{I}$.

4. Soft x-rays (E<300 eV) were observed 300-400 ns into the current pulse while harder x-rays (E $\sim$ 1 keV) were observed at 600-800 ns. The soft x-rays appear to be associated with m=0 sausage instabilities which were observed to be rapidly growing at that time. The excitation process associated with compressing and heating a plasma to high densities in a MHD pinch, augmented by radiative collapse, that has been proposed to occur for high z-pinches, may not operative here because of the density minima that is observed on axis in

76

the necks. These dense minima suggest a beam excitation process. The hard x-rays appear to be associated with inductive dips in the current waveform.

5. Studies of x-ray emission by layered Mg on Al loads on Double Eagle indicate that only 30-50% of the outside layer implodes on axis and contributes to the x-ray emission. These studies conclusively show that the outside surface of the load sluffs off and implodes over a period of time. These results along with two wire in-house studies provide a load straggling explanation for the longer than expected duration of the x-ray pulse. They also reconcile the observation that the calculated yield can account for the measured yield only if a small fraction of the original wire mass takes part in the emission process. Any sharing of the generator current between the imploded load mass and that remaining near the original wire position (and possibly imploding later) would represent electrical energy not transferred to the radiating. This could result in dramatic inefficiency.

In conclusion, the results demonstrate that a heterogeneous discharge channel is formed with the current flowing primarily in the hot corona surrounding a core that may be neutral well into the discharge. This discharge configuration is very important to the implosion dynamics of an array because of the nonuniform acceleration experienced at different locations in one current channel due to the magnetic field of the other wires. This nonuniform acceleration leads to a preemptive implosion of the core resulting in a dramatic decrease in coupling efficiency of the generator to the radiating portion of the load. The coupling of the generator to the load depends on the early time conductivity profile in the load region. Low density and high temperature plasmas, that are created when out gassed surface contaminants are ionized, can shunt large fractions of the current away from the load. Our results show the coupling efficiency to be poorer with the opening switch. This poor coupling may be due to out gassing caused by a very small prepulse current heating the wire or blow by plasma from the POS. The important issue in obtaining good coupling is avoiding highly conducting alternative paths for the current.

The results show that the sudden approximation, where the vapor phase of the wire is assumed to be of no consequence to the load dynamics is not a good approximation for the early start-up phase of the pinch. Thermal conductivity and non-Sptizer resistivity play an important role and must be considered. Modelling of array physics must include $r - \theta$ variation which allows parts of the load mass to separate and implode at different rates.

Future studies are required to determine how the current is divided between the precursor plasma and the residual core and how this division may be avoided.

APPENDIX
BIBLIOGRAPHY

1 N.R. Pereira and J. Davis,"X-Rays from Z-Pinches on Relativistic Electron-Beam Generators,"(UNCLASSIFIED) J. Appl. Phys. **64**, R1 (1988).(UNCLASSIFIED)

2 C. Stallings, K. Nielson, and R. Schneider,"Multiple-Wire Array Loads for High-Power Pulse Generators,"(UNCLASSIFIED) Appl. Phys. Lett. **29**, 404 (1976).(UNCLASSIFIED)

3 S.M. Galberg and A.L. Velikovich,"Suppression of Rayleigh-Taylor Instabilities by the Snowplow Mechanism,"(UNCLASSIFIED) Phys. Fluids **B5**, 1164 (1993).(UNCLASSIFIED)

4 F.J. Wessel, B. Etlicher, N.S. Edison, A.S. Chuvatin, L. Veron, C. Rouille, and S. Attelan,"Stabilization in Z-Pinch Plasmas Using Magnetic Fields," (UNCLASSIFIED)Amer. Phys. Soc. Bull., (1992).(UNCLASSIFIED)

5 F.J. Wessel, B. Etlicher, and P. Choi,"Implosion of an Aluminum Plasma Jet onto a coaxial Wire: A Z-Pinch with Enhanced Stability and Energy Transfer,"(UNCLASSIFIED) Phys. Rev. Lett. **69**, 3181 (1992).(UNCLASSIFIED)

6 S.J. Stephanakis, J.P. Apruzese, P.C. Burkhalter, J. Davis, R.A. Meger, S.W. McDonald, G. Mehlman, P.F. Ottinger, and F.C. Young,"Effect of Pulse Sharpening on Imploding Neon Z-Pinch Plasmas,"(UNCLASSIFIED) Appl. Phys. Lett. **48**, 829 (1986).(UNCLASSIFIED)

7 H.W. Bloomberg, M. Lampe, and D.G. Colombant,"Early Expansion in Exploding Multiple Wire Arrays,"(UNCLASSIFIED) J. Appl. Phys. **51**, 5277 (1980).(UNCLASSIFIED)

8 C. Deency, T. Nash, R.R. Prasad, L. Warren, K.G. Whitney, J.W. Thornhill, and M.C. Coulter,"Role of the Implosion Kinetic Energy in Determining the Kilovolt X-Ray Emission from Aluminum-Wire-Array Implosions,"(UNCLASSIFIED) Phys. Rev. **A44**, 6762 (1991).(UNCLASSIFIED)

9 J. Guiliani, Private Communication.(UNCLASSIFIED)

10 R.B. Spielman,"Stagnation Dynamics and Heating Mechanisms for Wire Array Z-Pinch Implosions,"(UNCLASSIFIED) Third Int. Conf. on Dense Z-pinches, London, UK (April 19-29, 1993).(UNCLASSIFIED)

11 I.R. Lindemuth, G.H. McCall, and R.A. Nebel,"Fiber Ablation in the Solid-Deuterium Z-Pinch,"(UNCLASSIFIED) Phys. Rev. Lett. **62**, 269 (1989).(UNCLASSIFIED)

12 N.A. Bobrova, T.L. Razinkova, and P.V. Sasarov,"Electrical Explosion of Frozen Deuterium Filaments,"(UNCLASSIFIED) Sov. J. Plasma Phys. **18**, 269 (1992).(UNCLASSIFIED)

13 L.E. Aranchuk, G.S. Bogolyubskii, G.S. Volkov, V.D. Korolev, Yu. V. Koba, V.I. Linsonov, A.A. Lukin, L.B. Nikandrov, O.V. Tel'kovslaya, M.V. Tilupov, A.S. Cherenko, V. Ya. Tsarfin, and V.V. Yankov,"Radiatively Cooled Z-Pinch Produced by an Exploding Copper Wire,"(UNCLASSIFIED) Sov. J. Plasma Phys. **12**, 765 (1986).(UNCLASSIFIED)

14 I.K. Aivozov, V.D. Vikarev, G.S. Volkov, L.B. Nikandrov, V.P. Smirnov and V.Ya. Tsarfin,"Formation of Axial Foreplasma Channel in the Initial Slope of the Compression of a Multiwire System by Megampre Currents(Experimental),"(UNCLASSIFIED) Sov. J. Plasma Phys. **14**, 110 (1988).(UNCLASSIFIED)

15 J. Bailey, Y. Ettinger, A. Fisher, and N. Rostoker,"Gas-Puff Z-Pinches with D_2 and D_2-Ar Mixtures,"(UNCLASSIFIED) Appl. Phys. Lett. **40**, 460 (1982).(UNCLASSIFIED)

16 V.V. Neudachin and P.V. Sasorov,"Magnetohydrodynamic Instabilities of Radiating Z-Pinches,"(UNCLASSIFIED) Nuclear Fusion **31**, 1053 (1991).(UNCLASSIFIED)

17 E.S. Figura, G.H. McCall, and A.E. Dangor,"Characteristics of a Z-Pinch Produced from a Glass Optical Fiber,"(UNCLASSIFIED) Phys. Fluids **B3**, 2835 (1991).(UNCLASSIFIED)

18 G. Parker and D.L. Peterson, Private Communication.(UNCLASSIFIED)

19 N.F. Roderick, Private Communication.(UNCLASSIFIED)

20 J. Giuliani, Jr., J.E. Rogerson, C. Deeney, T. Nash, R.R. Prasad, and M. Krishnan,"Aluminum Wire Array Implosions: Comparison of Experiments and Simulation,"(UNCLASSIFIED) JQSRT **44**, 471 (1990).(UNCLASSIFIED)

21 E.M. Epperlein and M.G. Haines,"Plasma Transport Coefficients in a Magnetic Field by Direct Numerical Solution of the Fokker-Plank Equation,"(UNCLASSIFIED) Phys. Fluids **29**, 1029 (1985).(UNCLASSIFIED)

22 R. Cauble, F.J. Rogers, and W. Rozmus,"An Analytic Expression for Electrical Resistivity in Near-Solid Density, Laser-Produced Plasmas,"(UNCLASSIFIED) SPIE bf 1229, (1990).(UNCLASSIFIED)

23 A. Fisher, Private Communication.(UNCLASSIFIED)

24 D.R. Kania,"Device for Loading Thin Wires in a Vacuum,"(UNCLASSIFIED) Rev. Sci. Instrum. **55**, 39 (1984).(UNCLASSIFIED)

25 B.K.F. Young, R.E. Stewart, and J.G. Woodworth,"Experiment Demonstration of a 100-ps Microchannel Plate Framing Camera,"(UNCLASSIFIED) Rev. Sci. Instrum. **57**, 2729 (1986).(UNCLASSIFIED)

26 F.C. Jahoda, R.A. Jeffries, and G.A. Sawyer,"Fracional-Fringe Holographic Plasma Interferometry,"(UNCLASSIFIED) Applied Optics 6, 1407 (1967).(UNCLASSIFIED)

27 I.H. Hutchinson, *Principles of Plasma Diagnostics*, Cambridge Univ. Press, Cambridge MA, pp. 95, 1992.(UNCLASSIFIED)

28 K. Bockasten,"Transformation of Observed Radiances into Radial Distribution of the Emission of a Plasma,"(UNCLASSIFIED) J. Opt. Soc. **51**, 943 (1961).(UNCLASSIFIED)

29 F.C. Young, S.J. Stephanakis, and V.E. Scherrer,"Filtered X-Ray Diodes for Imploding Plasma Experiments,"(UNCLASSIFIED) Rev. Sci. Instrum. **57**, 2174 (1986).(UNCLASSIFIED)

30 R.B. Spielman, W.W. Hsing, and D.L. Hanson,"Photoconducting X-Ray Detectors for Z-Pinch Experiments,"(UNCLASSIFIED) Rev. Sci. Instrum. **59**, 1804 (1988).(UNCLASSIFIED)

31 C.M. Vest, *Holographic Interferometry*, John Wiley & Sons, NY, pp. 355, 1979.(UNCLASSIFIED)

32 F.C. Jahoda and G.A. Sawyer,"Optical Refractivity of Plasmas,"(UNCLASSIFIED) in *Methods of Experimental Physics*(UNCLASSIFIED) Vol. 9-Part B Plasma Physics, H.R.

Griem and R.H. Lovberg,ed., Academia Press, NY and London, pp. 1, 1971.(UNCLAS-SIFIED)

33 J. Apruzese, Private Communication.(UNCLASSIFIED)

34 P. Sheehey, J.E. Hammel, I.R. Lindemuth, D.W. Scudder, J.S. Shlacter, R.H. Lovberg, and R.A. Riley, Jr.,"Two-Dimensional Direct Simulation of Deuterium Fiber-Initiated Z-Pinches with Detailed Comparison to Experiment,"(UNCLASSIFIED) Phys. Fluids **B4**, 3698 (1992).(UNCLASSIFIED)

35 D. Mosher and D. Colombant,"Pinch Spot Formation in High Atomic Number Z Discharges,"(UNCLASSIFIED) Phys. Rev. Lett. **68**, 2600 (1992).(UNCLASSIFIED)

36 B.A. Trubmikov,"Particle Acceleration and Neutron Production at the Necks of Plasma Pinches,"(UNCLASSIFIED) Sov. J. Plasma Phys. **12**, 271 (1986).(UNCLASSIFIED)

37 D.H. Kalantar and D.A. Hammer,"Dynamics of an X-Pinch Plasma from Time Resolved Diagnostics,"(UNCLASSIFIED) *3rd Inter. Conf. on Dense Z-pinches,* Imperial College, London, UK (April 19-28, 1993).(UNCLASSIFIED)

38 J. Pearlman, W. Clark, and E. Chu,*Proceedings of the Fourth Inter. Topical Conf. on High Power Electron and Ion Beam Research and Technology,* Palaiseau, France, pp. 255 (1981).(UNCLASSIFIED)

39 B.L. Henke, J.Y. Uejio, G.F. Stone, C.H. Dittmore, and F.G. Fujiwara,"High Energy X-Ray Response of Photographic Films: Models and Measurements,"(UNCLASSIFIED) J. Opt. Soc. Amer. **B3**, 1540 (1986).(UNCLASSIFIED)

40 G.V. Marr, *Plasma Spectroscopy*(UNCLASSIFIED), Elsevier, Amsterdam, p. 267, 1968.(UNCLASSIFIED)

DEPARTMENT OF DEFENSE

ASSISTANT TO THE SECRETARY OF DEFENSE
    ATTN: EXECUTIVE ASSISTANT

DEFENSE INTELLIGENCE AGENCY
    ATTN: DGI4

DEFENSE NUCLEAR AGENCY
    ATTN: DFRA
    ATTN: DFRA JOAN MA PIERRE
    ATTN: DFTA GERDING
    ATTN: DFTD
2 CY ATTN: IMTS
    ATTN: PAO
    ATTN: PR MAJ KYME
    ATTN: RAEM K SCHWARTZ
    ATTN: RAES
    ATTN: RAES R C WEBB
    ATTN: RAES W J SCOTT
2 CY ATTN: RAST
    ATTN: RAST DR G DAVIS
    ATTN: RAST P HEBERT
    ATTN: SPSD MAJ K ZERINGUE
    ATTN: TAIC
    ATTN: TDSP
    ATTN: TDSP L PRESSLEY
    ATTN: TDTR

DEFENSE TECHNICAL INFORMATION CENTER
2 CY ATTN: DTIC/OC

FIELD COMMAND DEFENSE NUCLEAR AGENCY
    ATTN: FCT
    ATTN: FCTI
    ATTN: FCTT DR BALADI
    ATTN: FCTTR R W SHOUP

DEPARTMENT OF THE ARMY

ARMY RESEARCH LABORATORIES
    ATTN: TECH LIB
    ATTN: A POIRIER
    ATTN: G HUTTLIN
    ATTN: J CORRIGAN
    ATTN: SLCHD-NW-RS

PED MISSILE DEFENSE SFAE-MD-TSD
    ATTN: CSSD-AT I MERRITT
    ATTN: CSSD-ES-E R CROWSON
    ATTN: CSSD-ES-EY G POLLOCK
    ATTN: CSSD-WD D BRADSHAW

U S ARMY CORPS OF ENGINEERS
    ATTN: CERD-M DR LEVERENZ

U S ARMY NUCLEAR & CHEMICAL AGENCY
    ATTN: MONA-NU DR D BASH

U S ARMY TRADOC ANALYSIS CTR
    ATTN: ATRC-WSS-R

DEPARTMENT OF THE NAVY

DEPARTMENT OF THE NAVY
    ATTN: CODE R41
    ATTN: E NOLTING
    ATTN: L MILES

NAVAL RESEARCH LABORATORY
    ATTN: CODE 4750 J SETHIAN
    ATTN: CODE 4770 D MOSHER
    ATTN: CODE 4770 G COOPERSTEIN
    ATTN: CODE 6654 DR C D BOND
    ATTN: D MOSHER CODE 4770

NAVAL SURFACE WARFARE CENTER
    ATTN: CODE H-21

SPACE & NAVAL WARFARE
    ATTN: LCDR J SMITH CODE 32M11
    ATTN: R WOODS CODE 32M12

DEPARTMENT OF THE AIR FORCE

PHILLIPS LABORATORY
    ATTN: D H HILLAND

SAN ANTONIO AIR LOGISTICS CTR
    ATTN: ALC/SW F CRISTADORO

SPACE SYSTEM DIVISION/XR
    ATTN: SMC/CC
    ATTN: SMC/CNJZ
    ATTN: SMC/CZEA
    ATTN: SMC/EN
    ATTN: SMC/MBSS
    ATTN: SMC/MGS
    ATTN: SMC/MJ
    ATTN: SMC/MT
    ATTN: SMC/XRX
    ATTN: XR/PLANS

SSP-27334 TRIDENT
    ATTN: J BURTLE
    ATTN: K TOBIN

USAF/AEDC
    ATTN. CAPT FRANK FAIRCHILD

DEPARTMENT OF ENERGY

LAWRENCE LIVERMORE NATIONAL LAB
    ATTN: J NUCKOLLS

LOS ALAMOS NATIONAL LABORATORY
    ATTN: J BROWNELL

SANDIA NATIONAL LABORATORIES
    ATTN: L D POSEY DIV 9351
    ATTN: L M CHOATE DEPT 5151
    ATTN: MARTIN FUNTES
    ATTN: ORG 9300 J E POWELL

ATTN: ORG 9303 W BEEZHOLD
ATTN: ORG 9341 M HEDEMANN
ATTN: ORG 9341 W BALLARD
ATTN: R E PEPPING DIV 6465
ATTN: TECH LIB 3141
ATTN: W BALLARD DIV 9341

U.S. DEPARTMENT OF ENERGY
OFFICE OF MILITARY APPLICATIONS
ATTN: C B HILLAND

OTHER GOVERNMENT

CENTRAL INTELLIGENCE AGENCY
ATTN: OSWR J PINA

DEPARTMENT OF DEFENSE CONTRACTORS

ADVANCED RESEARCH & APPLICATIONS CORP
ATTN: R ARMISTEAD

AEROSPACE CORP
ATTN: LIBRARY ACQUISITION
ATTN: T PARK

APTEK, INC
ATTN: T MEAGHER

BDM FEDERAL INC
ATTN: W BETOWT
ATTN: W LARRY JOHNSON

CALSPAN CORP/AEDC
ATTN: C JETT
ATTN: L S CHRISTENSEN

HUGHES AIRCRAFT COMPANY
ATTN: SCG-S41/B36G

HY-TECH RESEARCH CORP
2 CY ATTN: E J YADLOWSKY
2 CY ATTN: J J MOSCHELLA
2 CY ATTN: R C HAZELTON
2 CY ATTN: T B SETTERSTEN

JAYCOR
ATTN: J R MILLARD
ATTN: T FLANAGAN

JAYCOR
ATTN: CYRUS P KNOWLES
ATTN: R SULLIVAN

JAYCOR
ATTN: C ROGERS
ATTN: R POLL
ATTN: S ROGERS

KAMAN SCIENCES CORP
ATTN: D CALDWELL
ATTN: D JANSEN

KAMAN SCIENCES CORP
ATTN: CLAUDE FORE
ATTN: DASIAC
ATTN: E DRISCOLL

KAMAN SCIENCES CORPORATION
ATTN: DASIAC

LOGICON R & D ASSOCIATES
ATTN: B WEBSTER

MAXWELL LABORATORIES INC
ATTN: DR C DISMUKES
ATTN: DR G GURTMAN
ATTN: J M WILKENFELD
ATTN: WAISMAN

MAXWELL LABS
ATTN: WILLIAM H RIX

MAXWELL LABS, INC
ATTN: N LOTER

MISSION RESEARCH CORP
ATTN: J R HENLEY

PHYSICAL SCIENCES, INC
ATTN: JOHN F DAVIS
ATTN: S SEILER

PHYSICS INTERNATIONAL CO
ATTN: C STALLINGS
ATTN: J RIORDAN
ATTN: S L WONG

PULSE SCIENCES, INC
ATTN: I D SMITH
ATTN: P W SPENCE

SCIENCE APPLICATIONS INTL CORP
ATTN: W CHADSEY

THE AEROPSACE CORP
ATTN: M HOPKINS

W J SCHAFER ASSOCIATES, INC
ATTN: J ALCARAZ